Critical gravitational collapse with angular momentum. II. Soft equations of state

Carsten Gundlach
Mathematical Sciences, University of Southampton, Southampton SO17 1BJ, United Kingdom

Thomas W. Baumgarte
Department of Physics and Astronomy, Bowdoin College, Brunswick, Maine 04011, USA

(Received 15 December 2017; published 8 March 2018)

We study critical phenomena in the collapse of rotating ultrarelativistic perfect fluids, in which the pressure P is related to the total energy density ρ by $P = \kappa\rho$, where κ is a constant. We generalize earlier results for radiation fluids with $\kappa = 1/3$ to other values of κ, focusing on $\kappa < 1/9$. For $1/9 < \kappa \lesssim 0.49$, the critical solution has only one unstable, growing mode, which is spherically symmetric. For supercritical data it controls the black-hole mass, while for subcritical data it controls the maximum density. For $\kappa < 1/9$, an additional axial $l = 1$ mode becomes unstable. This controls either the black-hole angular momentum, or the maximum angular velocity. In theory, the additional unstable $l = 1$ mode changes the nature of the black-hole threshold completely: at sufficiently large initial rotation rates Ω and sufficient fine-tuning of the initial data to the black-hole threshold we expect to observe nontrivial universal scaling functions (familiar from critical phase transitions in thermodynamics) governing the black-hole mass and angular momentum, and, with further fine-tuning, eventually a finite black-hole mass almost everywhere on the threshold. In practice, however, the second unstable mode grows so slowly that we do not observe this breakdown of scaling at the level of fine-tuning we can achieve, nor systematic deviations from the leading-order power-law scalings of the black-hole mass. We do see systematic effects in the black-hole angular momentum, but it is not clear yet if these are due to the predicted nontrivial scaling functions, or to nonlinear effects at sufficiently large initial angular momentum (which we do not account for in our theoretical model).

DOI: 10.1103/PhysRevD.97.064006

I. INTRODUCTION

Since the pioneering numerical work of Choptuik [1] on the massless scalar field, Evans and Coleman [2] on the perfect fluid, and Abrahams and Evans [3] on vacuum collapse, it has been known that interesting things happen at the *black-hole threshold*: the codimension-one hypersurface in the space of regular initial data that separates supercritical data which eventually form a black hole from subcritical data which do not.

What happens there can be summarized as universality, a self-similar contraction phase during the time evolution, and power-law scaling of quantities such as the black-hole mass with distance to the black-hole threshold. An example of this is the famous formula for the black-hole mass M for supercritical data,

$$M(p) \sim (p - p_*)^\gamma, \tag{1}$$

where p is the parameter of a generic two-parameter family of initial data, $p = p_*$ is the critical parameter that identifies the black-hole threshold (we have assumed for definiteness that a black hole forms for $p > p_*$), and γ is the critical exponent. We refer the reader to Ref. [4] for a review and further references to the literature.

In this paper we extend our numerical study of the critical collapse of rotating perfect fluids with the linear, ultrarelativistic equation of state $P = \kappa\rho$ from the radiation gas case $\kappa = 1/3$ (see, e.g., Refs. [2,5,6]) to other values of κ, in particular to values $0 < \kappa < 1/9$ (see also Ref. [7] for a study of such fluids in spherical symmetry). We expect this to be interesting as then the spherically symmetric critical solution [8,9] has not one but two growing modes [10]: the familiar spherical one, plus an axial $l = 1$ mode that can be thought of as a spin-up under self-similar contraction. For $\kappa \gtrsim 0.49$ an $l = 2$ mode is expected to become unstable [10], but in this paper we focus on the $l = 1$ modes for rotating fluids.

To understand the relevance of a second unstable mode, we first go back to initial data restricted to spherical symmetry. The critical solution then has only one unstable mode and hence, assuming linearization stability, it must have a finite-sized attracting manifold of codimension one. In our matter model, all initial data either produce a black hole or disperse. We define the black-hole threshold in phase space as the hypersurface (codimension-one manifold)

which separates the data that collapse from those that disperse. As the critical solution neither collapses nor disperses (it is self-similar and produces a naked singularity), its initial data must lie on the black-hole threshold, and hence the black-hole threshold and the attracting manifold of the critical solution coincide at least near the critical solution. In fact, numerical results in spherical symmetry indicate that the attracting manifold of the critical solution is the entire black-hole threshold.

For generic spherically symmetric initial data sufficiently near the black-hole threshold, there are then three phases of the time evolution. In Phase 1, the solution moves a potentially long distance from its starting point to near the critical solution. In Phase 2, the solution is approximated by the critical solution Z_* plus linear perturbations. It leaves this phase when the amplitude of the single growing perturbation mode Z_0 has grown sufficiently large. We normalize Z_0 so that this occurs at amplitude ± 1. The moment when this happens sets an overall length scale: as Z_* is a self-similar contraction, the later Z_0 becomes nonlinear, the smaller the scale. In Phase 3 the evolution is again nonlinear, but as the intermediate Cauchy data at the start of Phase 3 are universal up to the overall scale, namely $Z_* \pm Z_0$, this third phase is also universal up to this overall scale and the sign of Z_0: $Z_* + Z_0$ evolves into a black hole, while $Z_* - Z_0$ disperses.

If we now consider generic initial data that are near the black-hole threshold and slightly nonspherical, and if all nonspherical modes are stable (i.e. for $\kappa > 1/9$ in our matter model), then essentially the same picture holds: deviations from spherical symmetry in Phase 1 are small and can be treated as linear perturbations simply because they are small in the initial data. They decay further in Phase 2. At the beginning of Phase 3 we now have data $Z_* \pm Z_0 + \delta Z_1$, where Z_1 is the most slowly damped axial $l = 1$ perturbation mode, and by assumption its amplitude δ is small. In Phase 3, angular momentum can then be treated as a linear perturbation of the nonlinear evolution of the spherical data $Z_* \pm Z_0$, right up to the formulation of a slowly rotating black hole (considered as a linear perturbation of Schwarzschild). We normalize Z_1 so that J/M^2 of the black hole equals δ. Because Z_1 is a decaying mode, $\delta \to 0$ as the initial data are fine-tuned to the black-hole threshold, and so the perturbative treatment of angular momentum is consistent in this limit. Our previous work on $\kappa = 1/3$ bore out this theory [5,6], but we also found that it made quantitatively correct predictions up to fairly large values of J/M^2—an example of the "unreasonable effectiveness" of perturbation theory.

Consider now the case where both Z_0 and Z_1 are growing modes (and there are no others—i.e. for $\kappa < 1/9$ in our matter model). Consider again initial data whose deviation from spherical symmetry is small enough to remain linear in Phase 1. However, the amplitude of Z_1 now grows during Phase 2. Therefore, its amplitude at the end of Phase 2 can become large as we fine-tune the initial data to the black-hole threshold. In Ref. [11] one of us concluded that the final outcome of Phase 3 would now depend not only on the sign in front of Z_0, but also on the value of δ. In particular, we expect that a black hole forms for $|\delta| < \delta_*$ (although the threshold value δ_* may be infinite) and that $J/M^2 = F_{J/M^2}(\delta)$ for some nontrivial "universal scaling function" F_{J/M^2} [11]. To linear order we still expect $F_{J/M^2}(\delta) \simeq \delta$, but when Z_1 is a growing mode, δ can become large, in which case higher-order terms in $F_{J/M^2}(\delta)$ affect J/M^2.

Moreover, if we fine-tune any one parameter in the initial data to the black-hole threshold, we will not fine-tune the initial amplitudes of both growing modes to zero, reaching some minimum initial amplitude somewhere near the black-hole threshold. Hence we formally expect to see a breakdown of scaling sufficiently close to the black-hole threshold. However, we cannot at the moment exclude the possibility that the black-hole mass and spin go to zero at the black-hole threshold anyway, since this might still happen if the universal scaling functions $F_M(\delta)$ and $F_J(\delta)$ for the mass and spin vanish at the black-hole threshold given by $\delta = \delta_*$.

With two growing modes, in principle we need to fine-tune two parameters in the initial data in order to make the initial amplitudes of Z_0 and Z_1 small. However, any initial data which have a reflection symmetry cannot have angular momentum, and so Z_1, which is associated with angular momentum, cannot arise. Hence if we choose one of our two parameters (call it q) such that the initial data have a reflection symmetry for $q = 0$ but not for $q \neq 0$, then we know *a priori* that setting $q = 0$ in the initial data will set the amplitude of Z_1 to zero, and we only need to fine-tune the other parameter (call it p) to also set the amplitude of Z_0 to zero [11].[1]

II. THEORY

A. The critical solution

For the perfect fluids considered here, the critical solution is continuously self-similar. The only physical length scale of this solution can then be expressed as $t_* - t$, where t is the proper time of an observer at the center, and t_* refers to the accumulation event, i.e. the instant of proper time at which the solution has contracted to zero radius. Any quantity of dimension L^n, where L represents a length scale, must therefore scale with $(t_* - t)^n$. Any nondimensional quantity becomes time independent when expressed in terms of spatial coordinates x that are dragged along with the self-similar contraction. Symbolically, we may therefore write nondimensional quantities associated with the

[1]Another matter model that admits a two-mode-unstable critical solution, even in spherical symmetry, is a harmonic map coupled to gravity [12]. In this model, the amplitude of one of the two growing modes can be set to zero *a priori* by maximizing charge density over mass density in the initial data.

critical solution as $Z_*(x)$. Since the only length scale $t_* - t$ depends on time, the critical solution evidently does not display any global length scale and is therefore completely scale invariant, or continuously self-similar. The length scale that determines, for example, the mass of black holes formed in supercritical evolutions is determined by the time when the solution starts to deviate significantly from the critical solution, and hence by the growing perturbations of the critical solution.

B. Spherically symmetric one-parameter families of initial data

We first focus on spherical symmetry and assume that the (nonrotating) initial data are parametrized by a single parameter p. In spherical symmetry, the critical solution has exactly one growing mode, which we denote by $Z_0(x)$. Singling out this growing mode, we may approximate the solution in Phase 2 (near self-similarity) as

$$Z(t,x) = Z_*(x) + \zeta_0(t) Z_0(x) + \cdots \tag{2}$$

Linear perturbations that grow on a constant time scale increase exponentially in the time t. Here, however, the time scale of growth is the scale of the self-similar solution, $t_* - t$, so that the amplitude ζ_0 of the perturbation satisfies an equation of the form

$$\frac{d\zeta_0}{dt} \propto \frac{\zeta_0}{t_* - t}. \tag{3}$$

Accordingly, the mode grows exponentially in the dimensionless time coordinate

$$\tau := -\ln \frac{t_* - t}{c_t L_0}, \tag{4}$$

where L_0 is an arbitrary fixed length scale, and c_t is a dimensionless universal constant. (In the following, we measure all dimensional quantities in units of L_0.) We may therefore write

$$\zeta_0 = P(p) e^{\lambda_0 \tau}, \tag{5}$$

where the factor $P(p)$ depends on the initial data, and where λ_0 is the Lyapunov exponent of the one unstable spherical perturbation. Since $P(p)$ must vanish for the critical solution parametrized by $p = p_{*0}$, where we have inserted a subscript 0 referring to zero rotation, we may expand to leading order as

$$P(p) = C_0(p - p_{*0}) + \cdots \tag{6}$$

The constant C_0 depends on the particular one-parameter family of initial data and its parametrization. For definiteness, we assume that a black hole forms for $P > 0$.

The scale of dimensional quantities formed in near-critical collapse is determined by the time at which perturbations become nonlinear, i.e. when the evolution transitions from Phase 2 to Phase 3. We normalize the linear perturbation mode $Z_0(x)$ so that the growing mode becomes nonlinear when $\zeta_0 = \pm 1$. This occurs at a time[2]

$$\tau_\sharp := -\frac{\ln |P(p)|}{\lambda_0}. \tag{7}$$

The corresponding length scale is

$$e^{-\tau_\sharp} = \frac{t_* - t_\sharp}{c_t} = |P(p)|^{\frac{1}{\lambda_0}}. \tag{8}$$

In supercritical evolutions, the mass of the black hole that then forms must be proportional to this length scale, or more precisely

$$M \simeq c_M (C_0(p - p_{*0}))^{\frac{1}{\lambda_0}}, \tag{9}$$

where we have inserted the expansion (6), and where c_M is a dimensionless universal constant. Hence the critical exponent γ_M for the black-hole mass in Eq. (1) is the inverse of the growth rate λ_0,

$$\gamma_M = \frac{1}{\lambda_0}. \tag{10}$$

By shifting the origin of τ, we set $c_M = 1$ in the following. (This leaves c_t as a dimensionless universal constant that we cannot set to one.)

In this paper we focus on perfect fluid matter with the linear, ultrarelativistic equation of state

$$P = \kappa \rho, \tag{11}$$

where P is the pressure, ρ is the total energy density, and κ is a constant. A radiation fluid, in particular, is described by $\kappa = 1/3$. For such fluids, and for a given value of κ, the Lyapunov exponent λ_0 can be computed by perturbing the critical solution (see, e.g., Ref. [9], as well as Fig. 1).

It was first observed in Ref. [13] that critical scaling occurs in sub- as well as supercritical evolutions. In our matter model, by dimensional analysis, the maximum density attained in subcritical evolutions must scale with the inverse square of the length scale (8), so that for subcritical evolutions we may write

$$\rho_{\max} \simeq c_\rho (C_0(p_{*0} - p))^{\gamma_\rho} \tag{12}$$

with

[2]We note that $\tau_\sharp$ was called τ_* in our previous papers.

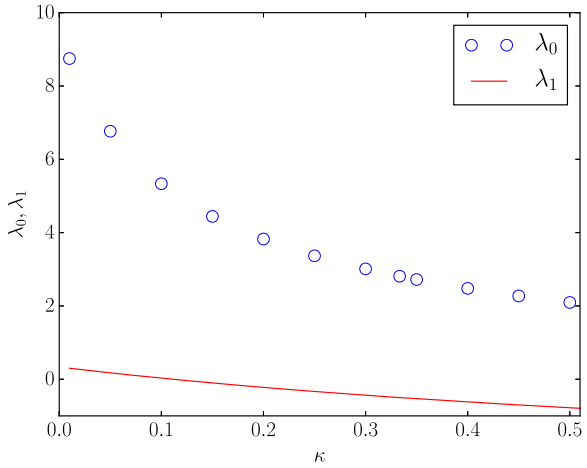

FIG. 1. Perturbative values of the Lyapunov exponents λ_0 and λ_1 for perfect fluids with the equation of state (11). The values for λ_0 are taken from Ref. [9], while the values for λ_1 are given by Eq. (17). The exponent λ_1 changes sign at $\kappa = 1/9$, reflecting the fact that the Z_1 mode becomes unstable for $\kappa < 1/9$. The values of λ_0 are much greater than those of λ_1 in this regime, which explains why the effects of Z_1 becoming unstable are difficult to observe in numerical simulations.

$$\gamma_\rho = -\frac{2}{\lambda_0}, \tag{13}$$

and c_ρ is another dimensionless universal constant.

C. Two-parameter families of rotating initial data

We now consider rotating initial data, and assume that these data are analytic and parametrized by two parameters p and $\mathbf{q}$. We further assume that, if these data evolve to form a black hole, the black-hole mass M and angular momentum $\mathbf{J}$ obey the symmetries

$$M(p, -\mathbf{q}) = M(p, \mathbf{q}), \tag{14a}$$

$$\mathbf{J}(p, -\mathbf{q}) = -\mathbf{J}(p, \mathbf{q}). \tag{14b}$$

A sufficient condition for these two assumptions to hold is that $\mathbf{q} \to -\mathbf{q}$ corresponds to a spatial reflection of the initial data. The assumption (14b) implies that initial data with $\mathbf{q} = 0$ form a nonspinning black hole, but not that they are necessarily spherically symmetric. In the following, for simplicity of notation, we restrict to axisymmetry, so that the vectors $\mathbf{q}$ and $\mathbf{J}$ reduce to their components along the symmetry axis, which we call simply q and J.

Generalizing the approximation (2) for rotating data we now write the evolution in Phase 2 as

$$Z(x,\tau) \simeq Z_*(x) + \zeta_0(p,q,\tau)Z_0(x) + \zeta_1(p,q,\tau)Z_1(x) + (\text{other}) \text{ decaying modes}, \tag{15}$$

where Z_0 is the single growing spherical mode, and Z_1 is either the single growing $l = 1$ axial mode or the least damped such mode. In complete analogy to our treatment in Sec. II B the amplitudes of the modes are given by

$$\zeta_0 = P(p,q)e^{\lambda_0\tau}, \qquad \zeta_1 = Q(p,q)e^{\lambda_1\tau}, \tag{16}$$

where τ is again given by Eq. (4).

The Lyapunov exponent λ_1 can again be determined from perturbations of the critical solution [10]. Remarkably, for a perfect fluid with the equation of state (11), the result can be expressed in closed form as a function of κ,

$$\lambda_1 = \frac{1 - 9\kappa}{3 + 3\kappa} \tag{17}$$

(see Fig. 1). λ_1 changes sign at $\kappa = 1/9$, marking the transition from Z_1 being stable and damped for $\kappa > 1/9$ to unstable and growing for $\kappa < 1/9$.

From Eqs. (14a)–(14b) we see that the coefficients P and Q must be even and odd in q, respectively. Hence the equivalent of Eq. (6) must, to leading order, be

$$Q = C_1 q + \cdots \tag{18}$$

for some family-dependent constant C_1. The black-hole threshold within such a two-parameter family is a curve in the (p,q) plane that is symmetric under $q \to -q$, parametrized by

$$|q| = q_*(p) \Leftrightarrow p = p_*(|q|). \tag{19}$$

We can fine-tune the initial data to the black-hole threshold along any smooth one-parameter family of initial data that crosses the threshold, in practice by bisection. As explained above, we can also fine-tune to the attracting manifold of the critical solution by setting $q = 0$ and fine-tuning p to the black-hole threshold.

We define the "reduced parameters"

$$\bar{p} \coloneqq C_0(p - p_{*0}), \tag{20a}$$

$$\bar{q} \coloneqq C_1 q \tag{20b}$$

as shorthands. Expanding about $\bar{p} = \bar{q} = 0$, we approximate

$$P(\bar{p},\bar{q}) = \bar{p} - K\bar{q}^2 + \cdots, \tag{21a}$$

$$Q(\bar{p},\bar{q}) = \bar{q} + \cdots, \tag{21b}$$

where K is another family-dependent dimensionless constant. We found in Refs. [5,6] that including the $\bar{q}^2$ term is essential. Assuming $\bar{p}$ and $\bar{q}^2$ to be of the same

order of smallness, Eqs. (21a)–(21b) is a consistent truncation to leading order.

The parameters p and q stand for any generic parameters of the initial data that obey Eqs. (14a)–(14b). In our calculations they will be represented by η, which parametrizes the overall fluid density, and Ω, which controls the rotation rate.

D. Evolution near the critical solution

We assume now that P and Q have been chosen small enough so that, after an initial transition period (Phase 1), $\zeta_0 Z_0$ and $\zeta_1 Z_1$ can be treated as linear perturbations of Z_* over some range $\tau_2 \lesssim \tau \lesssim \tau_\sharp$ (Phase 2), before either perturbation has grown too much and the evolution becomes again nonperturbative (Phase 3). The starting value τ_2 of τ depends only weakly on the initial data (through the length scale of the initial data, rather than the degree of fine-tuning), and its value does not matter at this point. ($\tau = 0$ itself has no particular physical significance, as we have chosen the origin of τ to make $c_M = 1$.)

From Eq. (16), the combination

$$\delta := \zeta_1 |\zeta_0|^{-\epsilon}, \tag{22}$$

where

$$\epsilon := \frac{\lambda_1}{\lambda_0}, \tag{23}$$

is independent of τ in Phase 2. It is therefore a suitable measure of the relative amplitude of the two modes. In particular, δ is given in terms of the initial data (p, q) by

$$\delta = Q|P|^{-\epsilon}. \tag{24}$$

Any function of δ would of course also be independent of τ. The definition (22) is singled out by being odd in q and to leading order proportional to it. Hence any quantity that does/does not change sign under a spatial reflection (such as angular momentum and mass, respectively) must be odd/even in δ.

Many of the qualitative differences between having one or two unstable modes are a consequence of ϵ in Eq. (23) becoming positive when λ_1 becomes positive, so that δ in Eq. (24) diverges rather than going to zero as $|P| \to 0$. For a perfect fluid, however, ϵ is very small for the entire range $0 \le \kappa \le 1/9$, as can be seen from Fig. 1, so that these effects will be difficult to observe numerically.

E. Scaling laws for two unstable modes and universal scaling functions

We now derive the scaling laws that follow from the existence of a Phase 2 given by Eq. (15). In contrast to Ref. [6] we allow both λ_0 and λ_1 to be positive, and in contrast to Ref. [11] we explicitly treat the two unstable modes on an equal footing. As τ increases, one or both of Z_0 and Z_1 will become nonlinear at some $\tau = \tau_\sharp$. One possible criterion for this is

$$\frac{\zeta_0^2(\tau_\sharp)}{b_0^2} + \frac{\zeta_1^2(\tau_\sharp)}{b_1^2} = 1, \tag{25}$$

where b_0 and b_1 are two universal dimensionless constants. We extend our convention from the nonrotating case to normalize the mode $Z_0(x)$ so that $b_0 = 1$, that is, nonlinearity is given by

$$\zeta_0^2(\tau_\sharp) + \frac{\zeta_1^2(\tau_\sharp)}{b_1^2} = 1, \tag{26}$$

but we retain a nontrivial value of $b_1 > 0$ in the following. Adopting this criterion and using Eq. (16), $\tau_\sharp(p, q)$ is given implicitly by

$$P^2 e^{2\lambda_0 \tau_\sharp} + \frac{Q^2 e^{2\lambda_1 \tau_\sharp}}{b_1^2} = 1. \tag{27}$$

The evolution of the two perturbation modes in the $\zeta_1\zeta_0$ plane during Phase 2 is represented in Fig. 2 for the case $\kappa = 0.08$. The thin lines show evolution trajectories in this plane, i.e. lines of constant δ as defined in Eq. (22). As we have $\lambda_1 > 0$, both modes grow with τ.

Phase 2 ends when the perturbations have grown sufficiently to reach a point on the nonlinearity ellipse (26), marked by a thick line. The location on the nonlinearity ellipse can be parametrized by an angle. We can introduce such an angle by identifying ζ_0 in Eq. (26) with $\cos\alpha$ and ζ_1/b_1 with $\sin\alpha$. In Fig. 2, we also schematically show the nonlinearity ellipse in the $\zeta_1\zeta_0$ plane. The shape of the *nonlinearity ellipse* is only schematic as we do not currently know the true value of b_1. Therefore we have simply assumed a value that makes for a clear plot and is not in conflict with our numerical results. (By contrast, we do have a theoretical result for the value of ϵ, which alone determines the shape of the *trajectories*.)

We may now express the Cauchy data at the start of Phase 3 of the evolution in two pieces: a scale-invariant part parametrized by α,

$$Z = Z_* + \cos\alpha Z_0 + b_1 \sin\alpha Z_1, \tag{28}$$

together with an overall length scale given by $e^{-\tau_\sharp}$. From Eq. (22) we see that the angle α is related to δ by

$$\delta = b_1 \sin\alpha |\cos\alpha|^{-\epsilon}. \tag{29}$$

The range $-\infty < \delta < \infty$ corresponds to the range $-\pi/2 < \alpha < \pi/2$ for $P > 0$, and separately to the range $\pi/2 < \alpha < 3\pi/2$ for $P < 0$. There is, however, a one-to-one

correspondence between values of the angle α and values of the pair (s,δ), where $s=\pm 1$ is the sign of P, or equivalently the sign of ζ_0.

Dimensional analysis now shows that any dimensionless quantity related to Phase 3 can only depend on the dimensionless angle α, but not on the length scale $e^{-\tau_\sharp}$. In particular, and most importantly, whether Phase 3 forms a black hole or disperses can depend only on α. In the special case of spherical symmetry, we have that $\alpha=0$ results in a black hole, while $\alpha=\pi$ results in dispersion. We also know that perturbing spherically symmetric data with a sufficiently small amount of angular momentum does not change the final outcome (collapse or dispersion). Hence there must be a universal constant $0<\alpha_*<\pi$ (depending on the equation-of-state parameter κ) such that Phase 3 forms a black hole precisely for $-\alpha_*<\alpha<\alpha_*$ (the red part of the nonlinearity ellipse in Fig. 2), and disperses otherwise (the green part of the nonlinearity ellipse.) This in turn means that for initial data sufficiently close to both the black-hole threshold and $q=0$ for the evolution to have a Phase 2, the final outcome (collapse or dispersion) in Phase 3 depends only on $\alpha(p,q)$ given by Eq. (29) with Eq. (24).

Furthermore, the dimensionless quantities J/M^2 (for supercritical data) and $\omega_{\max}/\sqrt{\rho_{\max}}$ (for subcritical data) can only depend on α; that is, there must exist universal scaling functions $F_{\omega/\sqrt{\rho}}$ and F_{J/M^2} such that

$$\frac{J}{M^2}\simeq F_{J/M^2}(\alpha),\qquad -\alpha_*<\alpha<\alpha_*, \tag{30a}$$

$$\frac{\omega_{\max}}{\sqrt{\rho_{\max}}}\simeq F_{\omega/\sqrt{\rho}}(\alpha),\qquad \text{otherwise}. \tag{30b}$$

Here $\rho_{\max}$ is the maximum over the entire spacetime of the central density ρ_c, and $\omega_{\max}$ is the maximum of the central angular velocity ω_c defined below in Sec. III C.

Finally, any dimensional quantity characterizing Phase 3 must be given by a suitable power of the length scale $e^{-\tau_\sharp}$, times a universal scaling function of α. For supercritical evolutions these quantities include the black-hole mass M and angular momentum J, while for subcritical evolutions they include the maximum values taken by the central fluid density ρ_c and the central angular velocity ω_c. Hence we must have

$$M\simeq e^{-\tau_\sharp}F_M(\alpha), \tag{30c}$$

$$J\simeq e^{-2\tau_\sharp}F_J(\alpha), \tag{30d}$$

$$\rho_{\max}\simeq e^{2\tau_\sharp}F_\rho(\alpha), \tag{30e}$$

$$\omega_{\max}\simeq e^{\tau_\sharp}F_\omega(\alpha), \tag{30f}$$

where obviously F_M and F_J are defined only for $-\alpha_*<\alpha<\alpha_*$ and F_ρ and F_ω for the complementary range of α, and where $F_{J/M^2}=F_M/F_J^2$ and $F_{\omega/\sqrt{\rho}}=F_\omega/\sqrt{F_\rho}$.

We could express α_* in terms of the pair (s_*,δ_*). Similarly, we could replace the angle α as the argument of the universal scaling functions F by the pair (s,δ), but this would then require a pair of scaling functions $F_\pm(\delta)$. Another disadvantage of using (s,δ) is that, at $P=0$, δ is not a smooth parameter. By contrast, α can be smoothly continued across $P=0$, with $\alpha\pm\pi/2\simeq b_1^{-1/\epsilon}P$, and across $Q=0$, with $\alpha\simeq b_1 Q$ and $\pi-\alpha\simeq b_1 Q$.

F_M and F_ρ must be even functions of α (or δ), while $F\omega$, F_J, $F_{\omega/\sqrt{\rho}}$ and F_{J/M^2} are odd. Hence at $\alpha\simeq 0$ ($\delta\simeq 0$ with $P>0$), and using our previous conventions, to leading order we must have

$$F_M\simeq 1, \tag{31a}$$

$$F_J\simeq\delta\simeq b_1\alpha, \tag{31b}$$

$$F_{J/M^2}\simeq\delta\simeq b_1\alpha, \tag{31c}$$

while at $\alpha\simeq\pi$ ($\delta\simeq 0$ with $P<0$), we must have

$$F_\rho\simeq c_\rho, \tag{31d}$$

$$F_\omega\simeq c_\omega\delta\simeq c_\omega b_1(\pi-\alpha), \tag{31e}$$

$$F_{\omega/\sqrt{\rho}}\simeq\frac{c_\omega}{\sqrt{c_\rho}}\delta\simeq\frac{c_\omega}{\sqrt{c_\rho}}b_1(\pi-\alpha), \tag{31f}$$

where we have defined the shorthands $c_\rho:=F_\rho(\delta=0)$ and $c_\omega:=dF_\omega/d\delta(\delta=0)$. Figure 3 shows theoretical curves of constant δ in the $\Omega\eta$ plane of initial data for the two-parameter family of initial data described below, for $\kappa=0.08$. Note that, in contrast to the $\zeta_1\zeta_0$ plane in Fig. 2, these curves are not trajectories, as the time evolution of the initial data does not remain within our two-parameter family of initial data. To compute δ, we have used the definition (24) of δ in terms of P and Q, together with the leading-order approximations (21a)–(21b) of P and Q in terms of Ω and η, the known values of λ_0 and λ_1, and the numerically fitted values of the family-dependent parameters η_{*0}, C_0, C_1 and K. Hence these curves of constant δ are realistic approximations. In the same figure, we also show the one-parameter (sub)families of initial data by which we have explored our two-parameter family. This juxtaposition gives rise to constraints on δ_* and b_1 as follows.

First, the observed black-hole threshold in the $\Omega\eta$ plane is to good approximation a parabola out to $\Omega=0.3$. This means it is indistinguishable from what our prediction for the black-hole threshold would be for $\delta_*=\infty$. To make this more quantitative, we have plotted what the predicted black-hole threshold *would* be for $(s_*,\delta_*)=(+1,0.8)$ (the

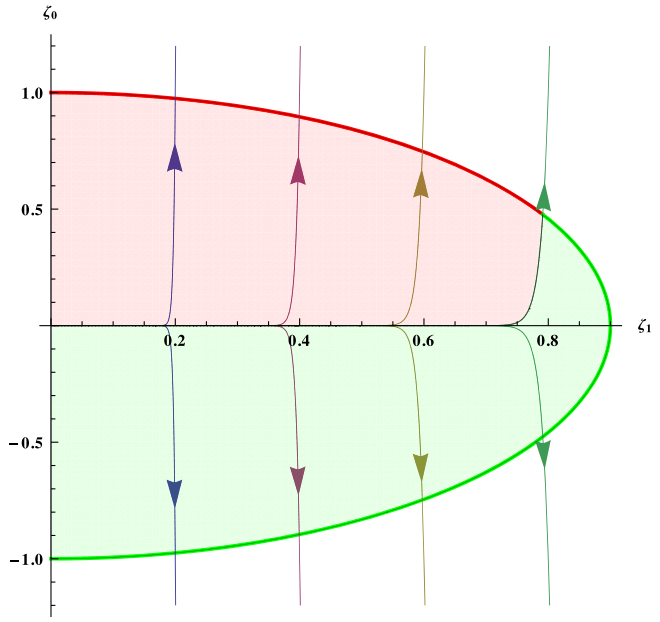

FIG. 2. The $\zeta_1\zeta_0$ plane of linear perturbations of the critical solution in Phase 2, for $\kappa = 0.08$. Only $\zeta_1 > 0$ is shown. The thin colored lines are lines of constant $\delta = 0.2$, 0.4, 0.6, 0.8, and mark trajectories of the perturbation amplitudes ζ_0 and ζ_1 during Phase 2. These trajectories are realistic because they depend only on the known parameter $\epsilon \simeq 0.0150$. The thick curve is a *schematic* representation of the nonlinearity ellipse (26). As we do not know the true values of the parameters b_1 and (s_*, δ_*), we have *arbitrarily* assumed $b_1 = 0.9$ and $(s_*, \delta_*) = (+1, 0.8)$. Data on the red segment of the nonlinearity ellipse form a black hole in Phase 3, while data on the green segment disperse. Any initial data that go through a Phase 2, and hence show critical scaling, must have initial values for (ζ_1, ζ_0) inside the nonlinearity ellipse. Hence evolutions that start Phase 2 in the red shaded region form a black hole in Phase 3, while evolutions that start Phase 2 in the green shaded region disperse in Phase 3.

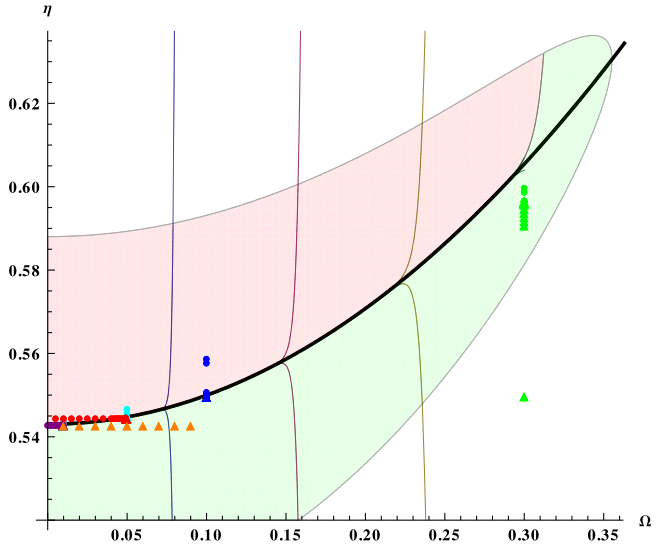

FIG. 3. The $\Omega\eta$ plane of initial data for $\kappa = 0.08$. The colored dots and triangles represent super- and subcritical data points, respectively, in our one-parameter families of initial data, color coded as in Table III. The thin colored curves represent $\delta = 0.2$, 0.4, 0.6, with the same color coding as in Fig. 2. The black parabola is the curve $\delta = \infty$. As discussed in the text, these curves are approximately realistic. We also *schematically* show which initial data *would* go through a Phase 2 and form a black hole (red shading), or go through a Phase 2 and disperse (green shading), for the arbitrarily assumed values $b_1 = 0.9$, $\delta_* = 0.8$ (as in Fig. 2), and $\tau_2 = 1.9$. As discussed in the text, the fact that the black-hole threshold is approximately a parabola out to $\Omega = 0.3$, shows that δ_* must be at least as large as assumed here, that is $\delta_* > 0.8$, and the fact that we still see scaling near the black hole at $\Omega = 0.3$ shows that the combination $e^{\lambda_1\tau_2}/b_1$ cannot be much smaller than that assumed here.

same arbitrary assumption we already made in Fig. 2). This hypothetical threshold turns up sharply just beyond $\Omega = 0.3$, and so is marginally compatible with our numerical observations, giving a hard constraint of $\delta_* \geq 0.8$ on δ_*. However, the specific value $\delta_* = 0.8$ we have chosen in Figs. 2 and 3 is for schematic illustration only.

Second, the region in the $\Omega\eta$ plane in which scaling is observed provides a (much less clear-cut) constraint on b_1. As before, we let τ_2 be the value of τ at the beginning of Phase 2. This value depends on the family of initial data, and within the family should depend smoothly on the initial data, and in particular it should vary little over data near the black-hole threshold. Then the condition that the evolution at τ_2 is still within the nonlinearity ellipse is that

$$P^2 e^{2\lambda_0\tau_2} + \frac{Q^2 e^{2\lambda_1\tau_2}}{b_1^2} < 1. \tag{32}$$

Hence data with (P, Q) that obey this condition will admit a Phase 2 and hence will be in the critical scaling regime. For given values of τ_2 and b_1, this defines an ellipse in the QP plane, and hence a deformed ellipse in the $\Omega\eta$ plane.

In Fig. 3 we have chosen arbitrary values $\tau_2 = 1.9$ and $b_1 = 0.9$ (the latter the same as in Fig. 2) that show the shape of this region clearly, while still being compatible with our observations of scaling at $\Omega = 0.3$. From this figure we see that the combination $e^{\lambda_1\tau_2}/b_1$ of τ_2 and b_1 cannot be much smaller than we have assumed here in order to make the shaded region extend all the way to $\Omega = 0.3$.

We stress again that the values of (s_*, δ_*), b_1 and τ_2 in Figs. 2 and 3, while compatible with our numerical observations, have been chosen primarily to give clear schematic plots of the shaded regions.

F. Review of the case of one unstable mode

At this point, it may be instructive to revisit the case $\epsilon < 0$ of a single unstable mode in the light of our notation for $\epsilon > 0$. There are several important qualitative differences.

First, Eq. (27) shows that for $\lambda_1 < 0$, $\tau_\sharp \to \infty$ as $P \to 0$ for any value of Q. This means that we can achieve

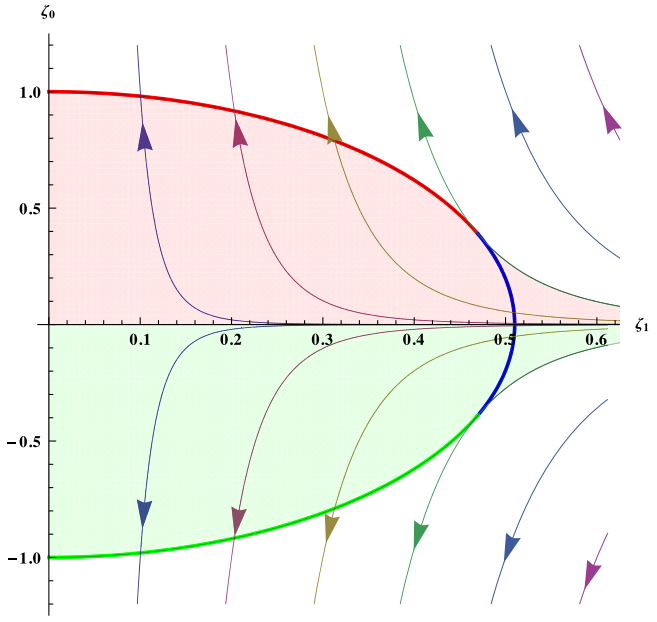

FIG. 4. The $\zeta_1\zeta_0$ plane of linear perturbations of the critical solution in Phase 2, for $\kappa = 1/3$. The thin colored lines are lines of constant $\delta = 0.1, 0.2, \ldots, 0.6$, and mark trajectories of the perturbation amplitudes ζ_0 and ζ_1 during Phase 2. We have used the known value $\epsilon \simeq -0.178$, and hence these curves are realistic. The thick curve is a *schematic* representation of the nonlinearity ellipse (26). As we do not know the true value of b_1, we have arbitrarily assumed that $b_1 = 0.51$, giving $\delta_{\max} \simeq 0.4$. Data on the red segment of the nonlinearity ellipse form a black hole in Phase 3, while data on the green segment disperse. Trajectories *enter* the nonlinearity ellipse across the blue segment. To show critical scaling, a time evolution must go through a Phase 2, that is, there must be an interval where it can be represented by a trajectory inside the nonlinearity ellipse. Hence evolutions that start in the red shaded region show scaling during Phase 2 and form a black hole in Phase 3, while evolutions that start in the green shaded region show scaling during Phase 2 and disperse in Phase 3. Note that the trajectories, and hence the boundary of the shaded regions, are only schematic outside the ellipse, as the evolution is nonperturbative there.

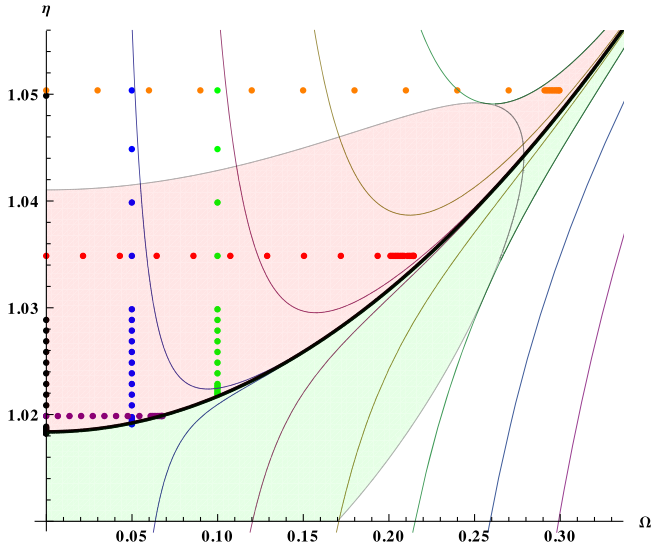

FIG. 5. The $\Omega\eta$ plane of initial data for $\kappa = 1/3$. We show the curves $\delta = 0.1, 0.2, \ldots, 0.6$, with the same color coding as in Fig. 4. We also show the one-parameter families of initial data used in Ref. [6], color coded as in Fig. 2 of Ref. [6]. (All these data are supercritical, and hence represented by dots.) The black-hole threshold is at $P = 0$, that is at $\delta = 0$ (thick black line). As discussed in the text, these curves are approximately realistic. We also *schematically* show the region of initial data space in which we *would* expect to see scaling under the arbitrary assumptions that $b_1 = 0.1$ (as in Fig. 4) and $\tau_2 = 1.8$. Any smaller value of b_1 would give a smaller $\delta_{\max}$ and would therefore be ruled out by the observation that we observe values of $\delta \simeq J/M^2$ up to 0.4 in the scaling regime.

arbitrarily small length scales $e^{-\tau_\sharp}$ with sufficient fine-tuning of P alone.

Second, Eq. (24) with $\epsilon < 0$ implies that $\delta \to 0$ as the black-hole threshold is approached and the approximations (31a)–(31f) become increasingly accurate.

Third, as illustrated by Fig. 4 for the case $\kappa = 1/3$, there is a trajectory in each quadrant of the $\zeta_1\zeta_0$ plane that just touches the nonlinearity ellipse $\zeta_0^2 + (\zeta_1/b_1)^2 = 1$. A simple calculation shows that in the upper right quadrant the touching point is at $\alpha = \alpha_{\max}$ given by

$$\alpha_{\max} := \operatorname{arccot}\sqrt{-\epsilon}, \tag{33}$$

and similarly in the other three quadrants. (For a given b_1, $\alpha_{\max}$ defines an equivalent $\delta_{\max}$.) Hence in the range $\alpha_{\max} < |\alpha| < \pi - \alpha_{\max}$ trajectories enter the nonlinearity ellipse, rather than leaving it. Therefore, α_* is not defined for $\epsilon < 0$. Rather, black holes form if and only if $\zeta_0 > 0$, that is $P > 0$, as illustrated in Fig. 4. The nonlinearity ellipse in this figure is only schematic, as we do not know the true value of b_1. For plotting, we have made the arbitrary assumption $b_1 = 0.51$, which, from Eqs. (33) and (29), yields $\delta_{\max} \simeq 0.4$. As we observed values of J/M^2 up to 0.4 in the scaling regime, and we approximate $J/M^2 \simeq \delta$ in the case of a single unstable mode, our assumed value of b_1 is just compatible with our observations, and we must have the constraint $b_1 \geq 0.51$.

Trajectories with $|\delta| > \delta_{\max}$ miss the nonlinearity ellipse altogether, meaning that there is no Phase 2 and hence no critical scaling. However, if we extrapolate the linear perturbation picture beyond its assumed region of validity to the entire $\zeta_1\zeta_0$ plane, then evolutions with arbitrarily large $|\zeta_1|$ will eventually enter the nonlinearity ellipse and go through a Phase 2, provided that $|\zeta_0|$ is sufficiently small, namely that $|\delta| < \delta_{\max}$. It is natural to assume that the linear perturbation picture is still a qualitatively correct description of the full nonlinear dynamics. This is assumed in Figs. 4 and 5 in extending the shaded regions beyond the original ellipses.

If the attracting manifold of the critical solution were identical with the entire black-hole threshold in the space of

initial data, we would see critical scaling in the time evolution of *all* data that are sufficiently close to the black-hole threshold, even though very far from initial data for the critical solution.

There is good numerical evidence that in spherical symmetry, for various types of matter, the attracting manifold of the critical solution is indeed the entire black-hole threshold, including initial data which are very far from the critical solution. Beyond spherical symmetry, this assumption can be true only in some local sense. To construct an obvious counterexample, a two-parameter family of axisymmetric initial data could consist of two blobs of fluids (rotating for $q \neq 0$) well separated along the symmetry axis, each of which might show critical phenomena, but separately at different threshold values of p. However, in a (potentially large) neighborhood of spherically symmetric initial data we expect the perturbative phase-space picture to be a qualitatively correct model of the full phase-space picture, that is, as far as the attracting manifold of the critical solution extends as a smooth submanifold of the space of initial data, its codimension must be given by the number of its unstable perturbation modes of the critical solution. Further away, it could end or change dimension in an unsmooth manner, for example in a caustic.

For the nonrotating scalar field this was shown in Ref. [14] (although their results also seem to indicate a second, nonspherical, unstable mode) and for the nonrotating radiation fluid in Ref. [15]. We leave to future work the question of how far the attracting manifold of the spherical critical solution extends into the space of initial data also for rotating perfect fluids (for the equations of state $1/9 < \kappa \lesssim 0.49$ where the critical solution has a single unstable mode).

G. Breakdown of scaling at sufficient fine-tuning

Returning now to the case of two unstable modes, by contrast, we have $\lambda_1 > 0$. Now, from Eq. (27), $\tau_\sharp \to \infty$ requires that P and Q are both fine-tuned to zero. This is consistent with the observation that, in the presence of two unstable modes, the attracting manifold of the critical solution has codimension two. Conversely, for any $Q > 0$, the length scale will remain finite even when P is fine-tuned to zero. Equation (27) gives $\tau_\sharp(P, Q)$ only in an implicit form, but we can obtain a rough explicit approximation by assuming that one of the two terms on the left-hand side of Eq. (27) always dominates, giving

$$(e^{-\tau_\sharp}) \simeq \max\left(|P|^{\frac{1}{\lambda_0}}, |Q/b_1|^{\frac{1}{\lambda_1}}\right). \tag{34}$$

In practice, we cross the black-hole threshold on one-parameter families of initial data on which Q remains finite but on which P changes sign. For such families we then have

$$(e^{-\tau_\sharp})_{\min} \simeq |Q/b_1|^{\frac{1}{\lambda_1}}. \tag{35}$$

Equivalently, along such families we expect a breakdown of scaling when P is small enough such that the second term on the left-hand side of Eq. (27) dominates, that is approximately for

$$|P| < |Q/b_1|^{\frac{1}{\epsilon}}. \tag{36}$$

Note, however, that the existence of a minimum of the overall length scale $e^{-\tau_\sharp}$ does not necessarily imply that M, J, $\rho_{\max}$ and $\omega_{\max}$ are finite on the black-hole threshold. Our theoretical model does not tell us the behavior of the scaling functions $F(\alpha)$ at α_*. Any or all of them could vanish there, or be finite. If they all vanish, this may mask the formal existence of the minimum of the overall length scale $e^{-\tau_\sharp}$ given by Eq. (35), although scaling would still break down, unless the scaling functions also approached zero as a power of $|\alpha| - \alpha_*$.

H. Leading-order power laws at the black-hole threshold

Returning to our discussion of the case of two unstable modes, it is possible that the black-hole threshold occurs at $P = 0$, i.e. $\delta_* = \infty$ and $\alpha_* = \pi/2$. This is not a given, however, and in this section we will discuss the form of leading-order power laws at the black-hole threshold without making this assumption, in contrast to Ref. [11].

For $\alpha_* \neq \pi/2$, or equivalently $\delta_* \neq \infty$, a generic one-parameter family of initial data crosses the black-hole threshold at nonzero Q and P (giving a finite $\delta = \delta_*$). However, because ϵ is so small, this will happen at a very small value of P, and it will be difficult to distinguish the point on a one-parameter family of initial data where it crosses the black-hole threshold at $|P| = |Q/\delta_*|^{1/\epsilon}$ from the point where $P = 0$ occurs. A different way of saying this is that near the black-hole threshold α changes very quickly along any generic one-parameter family of initial data, so that α_* [or equivalently (s_*, δ_*)] is difficult to determine from the location of the black-hole threshold; see Fig. 3.

In principle it would be possible to determine the universal constants α_* and b_1 and the universal scaling functions $F(\alpha)$ directly by evolving the one-parameter family of initial data (28) at the beginning of Phase 3. This, however, requires knowledge of the functions Z_*, Z_0 and Z_1 in a gauge adapted to our code, which we currently do not have. We instead evolve fine-tuned generic initial data, which, we assume, ultimately evolve into Eq. (28). This means that in testing our theoretical model against numerical data such as $M(p, q)$, we have to fit α_*, b_1 and the $F(\alpha)$, as well as (necessarily) the family-dependent functions $P(p, q)$ and $Q(p, q)$.

As a way around our ignorance of α_*, we slightly recast the theory in a way that relates more directly to observation, and in particular uses the fact that, in contrast to P and Q, the black hole threshold $p = p_*(|q|)$ is directly observable. We note that the scaling laws (30a)–(30f) do not change their form if we replace $\tau_\sharp$ as a measure of overall scale with

$$\tau_\flat := \tau_\sharp + y(\alpha). \tag{37}$$

In particular, we choose $y(\alpha)$ to be defined implicitly by

$$e^{-\lambda_0\tau_\flat} := \tilde{P} := P - s_*\left(\frac{|Q|}{\delta_*}\right)^{\frac{1}{\epsilon}} = P\left[1 - ss_*\left(\frac{|\delta|}{\delta_*}\right)^{\frac{1}{\epsilon}}\right]. \tag{38}$$

As defined before, s is the sign of P and (s_*, δ_*) is an alternative parametrization of α_*, so that $s_* = 1$ for $0 < \alpha_* < \pi/2$ and $s_* = -1$ for $\pi/2 < \alpha_* < \pi$. At the same time, instead of either α or δ we use

$$\tilde{\delta} := Q|\tilde{P}|^{-\epsilon} \tag{39}$$

as the argument of our scaling functions. This guarantees that $\tilde{P} = 0$ and $\tilde{\delta} = \infty$ at the black-hole threshold $(s, \delta) = (s_*, \delta_*)$. In the limit $\delta_* = \infty$ (or $\alpha_* = \pi/2$) we recover $\tilde{P} = P$ and $\tilde{\delta} = \delta$. It is easy to derive an explicit expression for $\tilde{\delta}(\delta, s_*, \delta_*)$ and an algebraic equation giving $y(\alpha)$ implicitly, but their exact forms do not matter here.

We may therefore write our scaling formulas as

$$M \simeq e^{-\tau_\flat}\tilde{F}_M(\tilde{\delta}), \tag{40a}$$

$$J \simeq e^{-2\tau_\flat}\tilde{F}_J(\tilde{\delta}), \tag{40b}$$

$$\rho_{\max} \simeq e^{2\tau_\flat}\tilde{F}_\rho(\tilde{\delta}), \tag{40c}$$

$$\omega_{\max} \simeq e^{\tau_\flat}\tilde{F}_\omega(\tilde{\delta}). \tag{40d}$$

For $|\delta| \ll \delta_*$, Eq. (38) gives $\tilde{P} \simeq P$, and hence $\tau_\sharp \simeq \tau_\flat$ and $\tilde{\delta} \simeq \delta$. The leading-order expressions for the $\tilde{F}(\tilde{\delta})$ at small $\tilde{\delta}$ are therefore the same as for the original scaling functions at small δ [Eqs. (31a)–(31f)].

Given a two-parameter family of initial data, the values of the family-dependent constants C_0 and C_1 are then fixed by imposing the conventions $\tilde{F}_M = 1$ and $d\tilde{F}_J/d\tilde{\delta} = 1$ at $\tilde{\delta} = 0$. The sign of C_0 is fixed by the convention that at $q = 0$ black holes form for $P > 0$.

For any one-parameter family of initial data that crosses the black-hole threshold at $\tilde{P} = 0$ but $Q \neq 0$, at the point (p_*, q_*), we have, from Eqs. (20a)–(20b) and (21a)–(21b),

$$\begin{aligned}\tilde{P} &\simeq C_0(p - p_*) + KC_1^2(q_*^2 - q^2)\\ &\simeq C_0(p - p_*) + 2KC_1^2 q_*(q_* - q),\end{aligned} \tag{41}$$

that is, to leading (linear) order $\tilde{P}$ is simply the distance to the black-hole threshold, a directly observed quantity.

In theory, we pay a price for this convenient reparametrization. For example, if M is actually finite at the black-hole threshold, $\tilde{F}_M$ must diverge there to compensate for the fact that $e^{-\tau_\flat}$ vanishes there. However, we do not see any indication of a breakdown of scaling in M, J, $\rho_{\max}$ or $\omega_{\max}$ at the level of numerical fine-tuning we can achieve, and so the parametrization of our initial data in terms of $\tilde{P}$ and $\tilde{\delta}$ has no downside in our applications.

We note that the expressions (40a)–(40d) do not form power-law scaling laws yet. However, for Q not too large and $\tilde{P}$ not too small, we will have small $\tilde{\delta}$ (or δ), and so we can use Eqs. (31a)–(31f) to obtain the leading-order power laws

$$M \simeq \tilde{P}^{\gamma_M}, \tag{42a}$$

$$\frac{J}{Q} \simeq \tilde{P}^{\gamma_J}, \tag{42b}$$

$$\rho_{\max} \simeq c_\rho(-\tilde{P})^{\gamma_\rho}, \tag{42c}$$

$$\frac{\omega_{\max}}{Q} \simeq c_\omega(-\tilde{P})^{\gamma_\omega}, \tag{42d}$$

where we have identified the critical exponents

$$\gamma_M = \frac{1}{\lambda_0}, \tag{43a}$$

$$\gamma_J = \frac{2 - \lambda_1}{\lambda_0}, \tag{43b}$$

$$\gamma_\rho = -\frac{2}{\lambda_0}, \tag{43c}$$

$$\gamma_\omega = -\frac{1 + \lambda_1}{\lambda_0}. \tag{43d}$$

(We assume again the convention that a black hole forms for $\tilde{P} > 0$.) Equations (42a)–(42d) generalize the scaling law (1) to rotating configurations. We also see that, in this limit, the dimensionless quantities become

$$\frac{J}{M^2} \simeq Q\tilde{P}^{-\epsilon}, \tag{44a}$$

$$\frac{\omega_{\max}}{\sqrt{\rho_{\max}}} \simeq \frac{c_\omega}{\sqrt{c_\rho}}Q(-\tilde{P})^{-\epsilon}. \tag{44b}$$

III. NUMERICS

A. Numerical code

We employ a numerical code that solves Einstein's equations, expressed in the Baumgarte-Shapiro-Shibata-Nakamura formalism [16–18], in spherical polar coordinates (details of our implementation can be found in Refs. [19,20]). The code makes no symmetry assumptions, and handles the coordinate singularities using a reference-metric formalism [21,22] together with a proper rescaling of all tensorial quantities.

For the simulations presented in this paper we adopt axisymmetry, simply by setting all derivatives with respect to the azimuthal angular variable φ to zero, and by using the smallest possible number of grid points in the φ direction. We also impose equatorial symmetry between the two hemispheres, and resolve one hemisphere with a very modest number of $N_\theta = 12$ angular grid points. Since all functions depend on the angle much more weakly than on the radius, we expect that the resulting numerical error is still relatively small (see Fig. 7 in Ref. [15] for a demonstration). We use $N_r = 312$ radial grid points, which are allocated logarithmically (see Appendix A in Ref. [15]), so that the ratio between the size of the innermost and the outermost grid cells is about 0.0021. During the evolution we compute a typical length scale of the solution at the origin from $l = (\rho/\partial_r^2\rho)^{1/2}$, and compare this length scale with the size Δ_r of the innermost radial grid cell. When Δ_r/l exceeds a certain tolerance (typically set to 0.05) we regrid, meaning that we move the outer boundary to a smaller location, and interpolate all grid functions to a new grid with the same grid number and logarithmic cell distribution. We regrid up to 10 times, moving the outer boundary from 72 (in our code units) to a minimum value of 12 in equal fractions. This ensures that the center of the simulations remains outside of the domain of dependence of the outer boundary for sufficiently long for a black hole to settle down (see Fig. 6 below).

As in Refs. [5,6] we carry out our simulations with a $1 + \log$ slicing condition for the lapse α [23] as well as the version of the Gamma-driver condition [24] presented in Ref. [25] for the shift vector β^i.

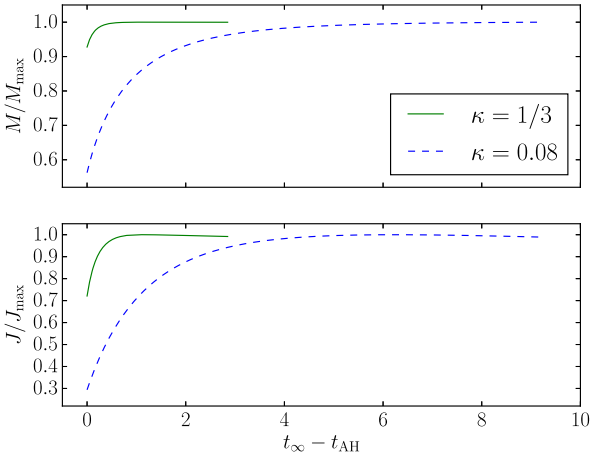

FIG. 6. The horizon mass M and angular momentum J, divided by their maximum values, as a function of coordinate time, which agrees with the proper time t_∞ as measured by a static observer at infinity. We denote with $t_{\rm AH}$ the time at which a horizon is first detected. We show examples for $\kappa = 1/3$ and $\kappa = 0.08$, both for $\Omega = 0.3$, and both for cases in which M is approximately 0.024 in our code units (namely $\eta = 1.0507$ for $\kappa = 1/3$ and $\eta = 0.596693$ for $\eta = 0.08$). For larger values of κ, the horizon mass and angular momentum change less after they are first formed, and settle down faster than for smaller values of κ.

B. Initial data

We adopt the same two-parameter family of initial data as in Refs. [5,6], except that we now allow for a general κ in the equation of state (11). Specifically, we set up a momentarily static spherically symmetric fluid ball with a Gaussian density distribution, centered on the origin, and parametrized by the central density η [see Eq. (6) in Ref. [5]]. We then endow this fluid with an angular velocity parametrized by Ω [see Eq. (7) in Ref. [5]] and solve the Hamiltonian and momentum constraints iteratively until the solution has converged to a desired tolerance. The parameters η and Ω are our specific instantiations of the parameters p and q used in Sec. II. Accordingly the amplitude of Z_1 must vanish for $\Omega = 0$.

We also set the shift to zero initially, and choose a "pre-collapsed" lapse $\alpha = \psi^{-2}$, where ψ is the conformal factor.

C. Diagnostics

We monitor a number of different quantities during our evolutions.

For supercritical evolutions we locate apparent horizons [26] and measure their irreducible mass $M_{\rm irr}$ and angular momentum J (see Ref. [27]). After a horizon is first formed, it grows for some time, as the newly formed black hole accretes more mass, but ultimately settles down to an equilibrium. From these equilibrium values of $M_{\rm irr}$ and J we determine the Kerr mass

$$M = M_{\rm irr}\left(1 + \frac{1}{4}\left(\frac{J}{M_{\rm irr}}\right)^2\right)^{1/2}. \tag{45}$$

For radiation fluids with $\kappa = 1/3$ we found that the black-hole masses increase by perhaps 10% or so after they are first formed, and that they settle down to equilibrium values rather quickly. For smaller values of κ, however, the black holes increase significantly more, and it also takes them significantly longer (measured in proper time at infinity), to settle down. In Fig. 6 we show examples for $\kappa = 1/3$ and $\kappa = 0.08$, both for $\Omega = 0.3$ and both for cases in which the horizon mass settles down to approximately 0.024 (in our code units). This behavior makes it considerably more challenging to analyze supercritical simulations for softer equations of state. Figure 6 also shows that the black-hole mass and angular momentum appear to decrease slightly after having passed through a maximum. This is a numerical artifact that is related to the finite numerical resolution of the black holes. The effect is more noticeable for smaller black holes, and contributes to the error in determining the black-hole parameters in particular close to the black-hole threshold. In practice, we adopt the maximum values of the black-hole mass and angular momentum as our best approximations.

The scaling of the black-hole angular momentum is mirrored by a characteristic of subcritical evolutions, namely the maximum angular velocity. In the axisymmetric

spacetimes considered here, a gauge-invariant measure of angular velocity is

$$\omega := \frac{\xi^a u_a}{\xi_a \xi^a} = \frac{u_\varphi}{g_{\varphi\varphi}}, \tag{46}$$

where $\xi = \partial/\partial\varphi$ is the rotational Killing vector, and u^a is the fluid four-velocity. We evaluate ω for the fluid worldline at the center, $r = 0$. For the initial data at $t = 0$, ω defined above agrees with the parameter Ω of the initial data.

IV. NUMERICAL RESULTS

From our two-parameter family of initial data with density parameter η and angular velocity parameter ω, we consider both "vertical" sequences for constant Ω, along which we vary η, and "horizontal" sequences for constant η, along which we vary Ω. These families appear as vertical and horizontal lines in Figs. 3 and 5, which illustrate the regions of parameter space that we explore for $\kappa = 0.08$ and $\kappa = 1/3$, respectively. Along each one of these sequences we locate the black hole threshold, and record M and J for supercritical data, as well as $\rho_{\max}$ and $\omega_{\max}$ for subcritical data. Most of our horizontal sequences are at constant $\eta > \eta_{*0}$, but we also take one horizontal sequence with constant $\eta < \eta_{*0}$, which does not cross the black-hole threshold. The black-hole threshold itself is approximately given by the parabola

$$C_0\eta_* \simeq K(C_1\Omega_*)^2 \tag{47}$$

(compare Refs. [5,6]) for the ranges of η and Ω that we have examined, even though small deviations can be seen in Figs. 3 and 5 for large values of Ω.

A. Overview of different κ

1. Nonrotating data

For nonrotating data with $\Omega = 0$ we have $Q = 0$ and hence, from Eq. (24), $\delta = 0$, independently of κ. For this special vertical sequence we may therefore adopt the power-law scalings (42a)–(42d) with

$$P \simeq C_0(\eta - \eta_{*0}) \tag{48}$$

from Eqs. (20a) and (21a) for any κ. The power law (42a) therefore becomes

$$M(\eta, 0) \simeq (C_0(\eta - \eta_{*0}))^{\gamma_M} \tag{49}$$

while Eq. (42c) becomes

$$\rho_{\max}(\eta, 0) \simeq c_\rho(C_0(\eta_{*0} - \eta))^{\gamma_\rho}. \tag{50}$$

Fitting our numerical data to these scalings determines the coefficients C_0, c_ρ as well as the critical exponents γ_M and γ_ρ, which we tabulate in Table I.[3] We find that our values agree to within a few percent with both analytical [9] and previous numerical results [7], and that $\gamma_\rho = -2\gamma_M$ within our estimated error, as expected from Eqs. (43a)–(43d).

Several factors contribute to the error in our data. In addition to the finite-difference error in our numerical simulations, including the uncertainties in determining the black-hole mass and angular momentum (see the discussion above), there is also some ambiguity in what data to include in the fits to the power laws (42a)–(42d). Data too far away from the black-hole threshold will no longer obey the power laws, while data too close will be affected more strongly by the finite-difference error for the very small structures formed during the collapse. This ambiguity alone leads to changes in the critical exponents of about a few percent, which we therefore adopt as an estimate of the error in our numerically determined critical exponents.

We next analyze both vertical and horizontal sequences for rotating data.

2. Rotating data

For $\kappa > 1/9$, we expect that, in the vicinity of the black-hole threshold, all characteristic variables can be described by the power-law scalings (42a)–(42d). We approximate

$$\tilde{P} \simeq C_0(\eta - \eta_*) \tag{51}$$

on our vertical sequences,

$$\tilde{P} \simeq KC_1^2(\Omega^2 - \Omega_*^2) \simeq 2KC_1^2\Omega_*(\Omega - \Omega_*) \tag{52}$$

on horizontal sequences with $\eta > \eta_{*0}$,

$$\tilde{P} \simeq C_0(\eta - \eta_{*0}) - K(C_1\Omega)^2 \tag{53}$$

on horizontal sequences with $\eta < \eta_{*0}$, and on all of these

$$Q \simeq C_1\Omega. \tag{54}$$

Inserting these expressions into Eqs. (42a)–(42d) we can make fits to our data to obtain the critical exponents (43a)–(43d) together with the threshold parameters $\eta = \eta_*(\Omega)$ and $\Omega = \Omega_*(\eta)$. We list our results in Table I. As expected, the threshold data lie approximately on the parabola (47).

From Eqs. (43a)–(43d) we see that we can also compute "heuristic" values of λ_0 and λ_1 from the numerically determined critical exponents. For supercritical data we find

$$\lambda_0 = 1/\gamma_M, \tag{55a}$$

$$\lambda_1 = 2 - \gamma_J/\gamma_M, \tag{55b}$$

while for subcritical data we find

[3]For these particular fits we fitted $\rho_{\max}^{-1/2}$ and $\omega_{\max}^{-1}$ to find the exponents $-\gamma_\rho/2$ and $-\gamma_\omega$, which are listed in Table I. The former in particular can then be compared directly with γ_M.

TABLE I. For each value of κ we list, in bold face, the analytical values of λ_0 (from Ref. [9]) and λ_1 [Eq. (17)] in the same row. For $\kappa = 0.08$, no analytical value for λ_0 is available, but, from interpolation, we approximate this value to be about 5.75. Also listed in these rows are the critical exponents γ as computed from Eqs. (43a)–(43d) obtained from fits to the expressions (40a)–(40d). All other rows contain our numerical data for the critical exponents γ for the corresponding values of κ. From these, we compute heuristic values of λ_0 and λ_1 from Eqs. (56a)–(56b) for subcritical data or Eqs. (55a)–(55b) for supercritical data. The entries N/A indicate that the fits were too poor to provide an accurate estimate for the critical exponents (see, e.g., Fig. 12 below). We list three significant digits for all numerically determined exponents, even though we estimate their relative errors to be on the order of a few percent.

		Subcritical data				Supercritical data			
Fixed parameter	Critical value	$-\gamma_\rho/2$	$-\gamma_\omega$	λ_0	λ_1	γ_M	γ_J	λ_0	λ_1
$\kappa = 0.5$		0.4774	0.1061	**2.095**	**−0.778**	0.4774	1.326	**2.095**	**−0.778**
$\Omega = 0$	$\eta = 1.09588$	0.475	⋯	2.11	⋯	0.484	⋯	2.07	⋯
$\Omega = 0.01$	$\eta = 1.0959$	0.476	0.103	2.05	−0.789	0.497	1.31	2.01	−0.636
$\Omega = 0.1$	$\eta = 1.0991$	0.488	0.103	2.05	−0.789	0.486	1.28	2.01	−0.634
$\Omega = 0.3$	$\eta = 1.1248$	0.482	0.109	2.07	−0.774	0.497	1.30	1.97	−0.616
$\kappa = 1/3$		0.3558	0.1779	**2.811**	**−0.5**	0.3558	0.8895	**2.811**	**−0.5**
$\Omega = 0$	$\eta = 1.01833$	0.356	⋯	2.81	⋯	0.358	⋯	2.79	−0.415
$\Omega = 0.01$	$\eta = 1.01836$	0.356	0.171	2.81	−0.519	0.357	0.862	2.80	−0.415
$\Omega = 0.1$	$\eta = 1.02198$	0.358	0.173	2.79	−0.517	0.356	0.861	2.81	−0.419
$\Omega = 0.3$	$\eta = 1.05058$	0.360	0.189	2.78	−0.475	0.361	0.898	2.77	−0.487
$\kappa = 0.2$		0.2614	0.203	**3.825**	**−0.222**	0.2614	0.581	**3.825**	**−0.222**
$\Omega = 0$	$\eta = 0.86926$	0.264	⋯	3.79	⋯	0.265	⋯	3.78	⋯
$\Omega = 0.01$	$\eta = 0.86930$	0.265	0.197	3.78	−0.257	0.264	0.561	3.79	−0.125
$\Omega = 0.1$	$\eta = 0.87381$	0.264	0.187	3.79	−0.292	0.265	0.575	3.78	−0.170
$\Omega = 0.3$	$\eta = 0.90830$	0.269	0.185	3.72	−0.312	0.271	0.628	3.69	−0.317
$\kappa = 0.1$		0.1875	0.1932	**5.333**	**0.03**	0.1875	0.3693	**5.333**	**0.03**
$\Omega = 0$	$\eta = 0.62203$	0.192	⋯	5.21	⋯	0.190	⋯	5.26	⋯
$\Omega = 0.01$	$\eta = 0.62210$	0.193	0.194	5.18	0.005	0.189	0.360	5.29	0.095
$\eta = 0.6236$	$\Omega = 0.049849$	0.197	0.178	5.08	−0.01	0.190	0.377	5.26	0.016
$\Omega = 0.05$	$\eta = 0.62361$	0.196	0.178	5.10	−0.09	0.190	0.381	5.26	−.005
$\Omega = 0.1$	$\eta = 0.62825$	0.197	0.156	5.07	−0.21	0.192	0.409	5.21	−0.13
$\Omega = 0.3$	$\eta = 0.67234$	0.198	N/A	5.05	N/A	0.192	0.430	5.21	−0.24
$\kappa = 0.08$		0.174	0.189	**5.75**	**0.086**	0.174	0.333	**5.75**	**0.086**
$\Omega = 0$	$\eta = 0.54302$	0.176	⋯	5.68	⋯	0.174	⋯	5.75	⋯
$\eta = 0.54309$	$\Omega = 0.009809$	0.179	0.186	5.59	0.039	0.172	0.319	5.81	0.145
$\Omega = 0.01$	$\eta = 0.54309$	0.183	0.193	5.46	0.055	0.173	0.317	5.78	0.167
$\eta = 0.5447$	$\Omega = 0.04922$	0.191	0.166	5.24	−0.13	0.174	0.337	5.75	0.063
$\Omega = 0.05$	$\eta = 0.54475$	0.183	0.162	5.46	−0.11	0.174	0.341	5.78	0.040
$\Omega = 0.1$	$\eta = 0.54982$	0.178	0.169	5.61	−0.05	0.178	0.353	5.61	0.017
$\Omega = 0.3$	$\eta = 0.59669$	0.189	N/A	5.29	N/A	0.178	0.389	5.61	−0.18

$$\lambda_0 = -2/\gamma_\rho, \tag{56a}$$

$$\lambda_1 = 2\gamma_\omega/\gamma_\rho - 1. \tag{56b}$$

The resulting heuristic values for λ_0 and λ_1 are also included in Table I.

We have found qualitatively similar effects for all $\kappa > 1/9$, but, for concreteness, we will focus on $\kappa = 0.2$ here.

For small Ω, we find good agreement of all exponents γ with the respective analytical values. Conversely, the heuristic values for λ_0 and λ_1 agree well with the theoretical ones. We note that the results for λ_1 have a larger *relative* error, when compared with the analytical values, than the exponents γ. This can be understood from the fact that λ_1 is relatively small, but, in Eqs. (55) and (56), it is computed from the difference of two numbers of order unity. Assuming that each γ has a relative error of 5%, say, will result in an *absolute* error in λ_1 of about 0.15 when computed from supercritical data, and about 0.05 when computed from subcritical data. Our data are within this range, at least for small Ω. Consistent with these estimates we find that, for small Ω, our heuristic values for λ_1 agree quite well with the theoretical values when computed from the subcritical data, but are somewhat larger than the theoretical values when computed from the supercritical data. We also show these results in Fig. 7, where supercritical (subcritical) data are shown as filled circles (triangles), and the theoretical values as crosses.

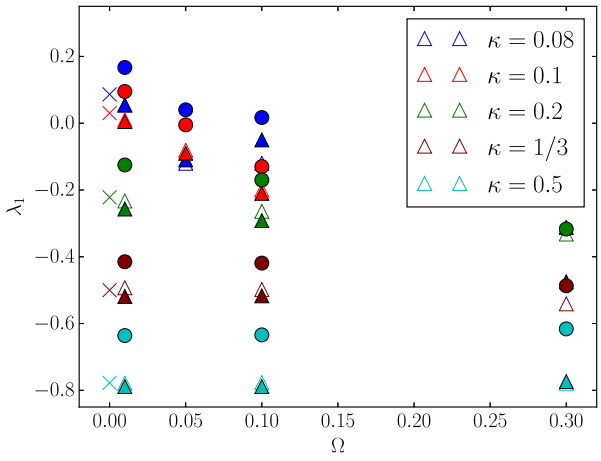

FIG. 7. Theoretical and heuristic values of λ_1. The crosses, plotted at $\Omega = 0$, represent the theoretical values given by Eq. (17). Filled circles (triangles) represent the results from power-law fits for the supercritical (subcritical) data tabulated in Table I. Open triangles represent dynamically determined values, obtained from fits to Eqs. (57) and (58) for near-critical evolutions. The subcritical and dynamical heuristic values agree well with the theoretical values for small Ω (and often cannot be distinguished in the figure). The supercritical heuristic values appear to overestimate λ_1, but, as discussed in the text, are also affected by a larger error. The heuristic values for λ_1 appear to be smaller than the theoretical ones for larger Ω, in particular for soft equations of state with small κ. As discussed in the text, several sources of error contribute to the uncertainty in these numbers, which therefore should be taken as estimates only.

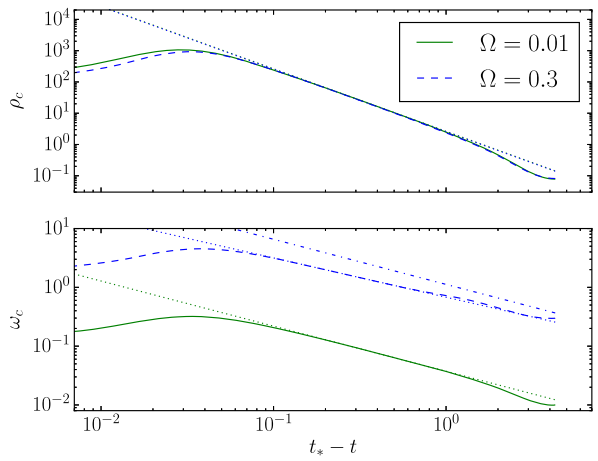

FIG. 8. The central density ρ_c (upper panel) and central rotation rate ω_c (lower panel) for subcritical evolution close to the black-hole threshold as a function of central proper time t, for $\kappa = 0.2$. Time advances to the left, as t approaches the time t_* of the accumulation event. The solid and dashed lines are numerical data, while the dotted lines are the fits (57) and (58) for the evolution during Phase 2. For comparison, we show the fit for $\Omega = 0.01$ scaled up by a factor of 30 in Ω to $\Omega = 0.3$, using the same heuristic λ_1 and d_ω (the dash-dotted line). This shows that over the dynamical range of $t_* - t$ that we see here, the increase in Ω appears to affect an overall scale in ω more than its scaling power.

Interestingly, however, we find that the fitted critical exponents change slightly when we increase Ω. For γ_ρ and γ_M these changes are quite small, and it is not clear whether they can be distinguished from numerical error. For γ_ω and γ_J, however, the changes are somewhat larger, and they appear to increase, for a given Ω, with decreasing κ. For a radiation fluid, with $\kappa = 1/3$, we also found a small increase in γ_J with Ω (see Table I in Ref. [5]), but all changes were well within the estimate of the numerical error. For $\kappa = 0.2$, the changes become more noticeable, with both γ_ω and γ_J increasing for larger Ω. Correspondingly, we find that the heuristic values of λ_1 also appear to change with Ω. For both subcritical and supercritical data we found that the heuristic values of λ_1 decrease with increasing Ω, i.e. become more negative. This trend can also be seen in Fig. 7.

We note that the authors of Ref. [14] also reported that, in nonspherical deformations of critical collapse with a scalar field, the critical exponent as well as the period of the discretely self-similar critical solution depend on the size of the deformation (see their Table I).

To our surprise we found that, at least for modest values of Ω, the above scaling laws model data quite accurately even for $\kappa < 1/9$. In the presence of two unstable modes, when $\lambda_1 > 0$ and hence $\epsilon > 0$, we can no longer assume that $\delta \to 0$ at the black-hole threshold [see Eq. (24)]. Accordingly, we are now probing the scaling functions for potentially large δ, so that the leading-order approximations (31a)–(31f) for the scaling functions may no longer apply, meaning that we also can no longer assume that the power-law scalings (42a)–(42d) hold. Nevertheless, we found surprisingly good agreement, especially if heuristic values are adopted for λ_1 which, as for $\kappa > 1/9$, decrease with increasing Ω.

3. Determination of λ_1 from time evolution

As an alternative approach to estimating an "effective" value of λ_1 we also examined the time evolution of the central density ρ_c and central angular velocity ω_c for near-critical initial data. Two examples, for $\kappa = 0.2$ with $\Omega = 0.01$ and $\Omega = 0.3$, are shown in Fig. 8. In the upper panel we show the evolution of the central density. We plot the data as a function of $t_* - t$, where t_* is the proper time of the accumulation event, so that time advances from right to left in the figure. The three phases of the evolution, which we described earlier, are clearly visible. In Phase 1 the data approach the critical solution. During Phase 2, the evolution follows the critical solution. On dimensional grounds, the density must be approximated by

$$\rho_c(t) \simeq d_\rho (t_* - t)^{-2} \tag{57}$$

where d_ρ is a universal constant during this part of the evolution. Fits to this scaling are included as the dotted line in the upper panel of Fig. 8. Phase 2 ends when perturbations of the critical solution become large; for the subcritical evolutions shown in Fig. 8 the density drops below that of the

critical solution. This is clearly visible in the left part of the figure.

The central rotation rate ω_c, shown in the lower panel of Fig. 8 would, from dimensional analysis alone, be expected to scale as $(t_* - t)^{-1}$. In addition, however, it also grows or decays with the mode Z_1 as $\exp \lambda_1 \tau \propto (t_* - t)^{\lambda_1}$. It should therefore be approximated by

$$\omega_c \simeq Q d_\omega (t_* - t)^{-1+\lambda_1} \tag{58}$$

where d_ω is a universal constant. In practice, we can now fit ρ_c during Phase 2 to the fit (57); this determines d_ρ and t_*. We then adopt this value of t_* in a fit of ω_c to Eq. (58). This allows us to determine λ_1 from the dynamical data. Admittedly these results for λ_1 have a significant error. One significant source of error is the time window over which the fits are performed, which should be restricted, of course, to Phase 2. We can nevertheless obtain estimates for λ_1, and interestingly these estimates are consistent with our observations based on the critical exponents described above.

The examples shown in Fig. 8 are for $\kappa = 0.2$ with $(\eta,\Omega) = (0.86930346, 0.01)$, and $(0.9082978, 0.3)$. The fit (57) for ρ captures properties of the unique critical solution, and therefore takes the same shape for both evolutions shown in the figure. For ω we can also identify an evolution well approximated by the fit (58) during Phase 2; however, even in the figure we notice that the two curves have a slightly different slope. For $\Omega = 0.01$ our fits suggest $\lambda_1 = -0.23$, while for $\Omega = 0.3$, we obtain $\lambda_1 = -0.33$. These values are quite similar to those obtained form the power-law fits to γ_ρ and γ_ω discussed above, and listed in Table I.

Using similar fits we estimated effective dynamical values of λ_1 for different values of κ and Ω; they are shown as open triangles in Fig. 7. In general, the trends discussed above appear to hold. The dynamical estimates for λ_1 agree quite well with those obtained from subcritical fits (filled triangles in Fig. 7). For small Ω, we also find good agreement with the theoretical values (17), shown as crosses in Fig. 7. For larger values of Ω however, the effective values appear to be smaller than the theoretical values. The changes are larger for smaller values of κ; in particular, for $\kappa = 1/3$ and 0.5 any changes appear to be well within the error of the data.

B. Example $\kappa = 0.08$

As a specific example of rotating collapse with $\kappa < 1/9$, we focus on $\kappa = 0.08$ in the remainder of this section. Even though we do not have an analytical value for λ_0 for this value of κ, it seems to be a good compromise between two competing effects: for smaller κ, the numerical simulations become increasingly challenging (see Sec. III C above), and for larger κ, closer to 1/9, ϵ becomes smaller.

We start by determining the different family-dependent parameters from the different power laws. Specifically, we initially determine η_{*0} and C_0 from $M(\eta)$ at $\Omega = 0$, C_1 from $J(\eta, \Omega)$ at small Ω, and K from the shape of the black-hole threshold. We then fit to the expressions (42a)–(42d). From these fits we determine the critical exponents as well as the threshold parameters η_* and Ω_*. The estimated values of the universal parameters for $\kappa = 0.08$, and of the family-dependent parameters of our two-parameter family of initial data are given in Table II. Our one-parameter sequences of data, together with their critical parameter values and color codings are given in Table III. In all of the following plots we will denote supercritical data with filled dots and subcritical data with filled triangles.

TABLE II. The parameters used in computing the theoretical fits for $\kappa = 0.08$ in the following figures.

parameter	status
$\lambda_0 = 1/\gamma_M \simeq 5.78$ $c_\rho \simeq 0.0065$ $c_\omega \simeq 0.144$ $\epsilon = \lambda_1/\lambda_0 \simeq 0.015$	universal but fitted
$\lambda_1 = 7/81 \simeq 0.0864198$	exact value used
$C_0 \simeq 0.0004$ $C_1 \simeq 2.15$ $K \simeq 0.00006$	family-dependent

TABLE III. Overview of the one-parameter sequences of data evolved for $\kappa = 0.08$. The grey and purple, and the cyan and red, families respectively cross the black-hole threshold at almost the same points. The critical values are used to evaluate $\ln|\tilde{P}|$ on the horizontal axes of the following figures. We will plot supercritical data as filled circles, and subcritical data as filled triangles.

fixed parameter	critical parameter	color
$\eta = 0.543$	all subcritical	orange
$\Omega = 0$	$\eta_* \simeq 0.54302320$	black
$\Omega = 0.01$	$\eta_* \simeq 0.5430926$	grey
$\eta = 0.54309$	$\Omega_* \simeq 0.009809$	purple
$\Omega = 0.05$	$\eta_* \simeq 0.54475323$	cyan
$\eta = 0.5447$	$\Omega_* \simeq 0.049219789$	red
$\Omega = 0.1$	$\eta_* \simeq 0.54981506$	blue
$\Omega = 0.3$	$\eta_* \simeq 0.59669136$	green

1. Limits on α_*

As mentioned above, we have hidden our ignorance of α_* [or (δ_*, s_*)] by using a degeneracy between the overall scale τ and the scaling functions F. This means that we will not be able to obtain information about α_* directly from the scaling laws. However, we do get a lower bound on δ_* from the fact that the black-hole threshold is approximately a parabola in the entire region of the $\Omega\eta$ plane that we have surveyed, as follows. In Fig. 3 we have plotted contours of δ, assuming that the leading-order approximations (21a)–(21b) are exact, and using our numerically determined values of C_0, C_1 and K. We see that for any value of $|\delta_*| < 0.8$ the black-hole

threshold would look qualitatively different, with the parabola either turning up at a sharp corner into an essentially vertical line (for $0 < \delta_* < 0.8$), or even turning sharply down into an essentially vertical line (for $-0.8 < \delta_* < 0$). We do not observe either behavior in the region of parameter space we have explored, and so we know that $\delta_* > 0.8$, with either sign of s_* possible. (This lower limit on $|\delta_*|$ corresponds to an upper limit on $|\alpha_* - (\pi/2)|$, but that limit also depends on the unknown value of b_1.)

2. Leading-order power laws

We test the expected leading-order scalings (40a)–(40d) in Figs. 9–12. We plot data and predictions for M, J/Ω, $\rho_{\max}$ and $\omega_{\max}/\Omega$ against $\ln|\tilde{P}|$.

The first thing that stands out is how good the leading-order power-law fits (with the exact λ_1 and the leading-order approximations to the scaling functions) are for most of our data. We do see some clear deviations from the power laws far from the black hole threshold (towards the right), where we have numerical data only for the $\Omega = 0$ (black) and $\Omega = 0.3$ (green) sequences. We are content to dismiss these as the theory breaking down far from the black-hole threshold.

We do not see any clear systematic deviation close to the black-hole threshold (towards the left) that would indicate nontrivial universal scaling functions for M or ρ. We do, however, see that the numerical data for both J and $\omega_{\max}$ at large initial angular momentum, namely for $\Omega = 0.1$ (blue) and $\Omega = 0.3$ (green), are both lower and steeper than the theoretical predictions. As discussed above, in the context of Table I for different equation-of-state parameters κ, both effects can be captured by assuming, in a purely heuristic manner, that an effective value of λ_1 decreases with increasing Ω. We show this in Figs. 10 and 12 as the dashed theoretical lines. For the supercritical data we find good agreement assuming heuristic values of $\lambda_1 = 0.017$ for $\Omega = 0.1$ and $\lambda_1 = -0.18$ for $\Omega = 0.3$—the same values as those listed in Table I. (Note that we have not adjusted the value of C_1.)

Finally, the data for $\Omega = 0.3$ (green) do no longer appear to follow a power law. The departure from a power law is very clearly visible for $\omega_{\max}$, but it is also present in M, J and $\rho_{\max}$. We have no plausible theoretical interpretation for this behavior. It is possible that these data are sufficiently far away from the critical solution that predictions based on linear perturbations of the critical solutions fail, but we also cannot rule out that this behavior represents a numerical artifact. Accordingly, we did not list values for γ_ω in Table I for $\Omega = 0.3$ and $\kappa < 1/9$.

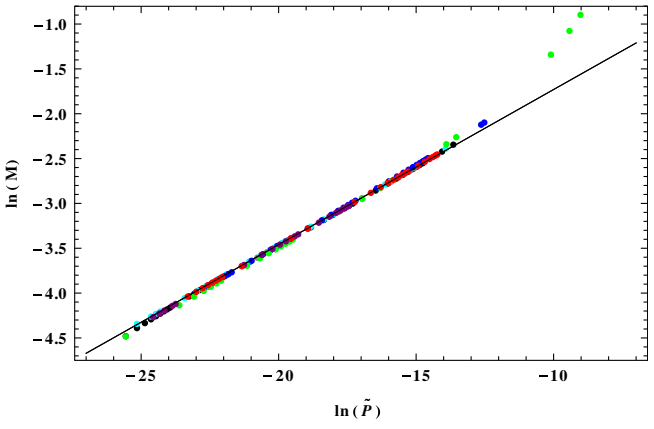

FIG. 9. Leading-order scaling of the black-hole mass M. The colored dots show numerical results for $\ln M$, plotted against $\ln\tilde{P}$. $\tilde{P}(\Omega,\eta)$ has been computed from Eq. (51) for vertical sequences and from Eq. (52) for horizontal sequences. The parameters and color codings are given in Tables II and III. The solid black line is the theoretical prediction.

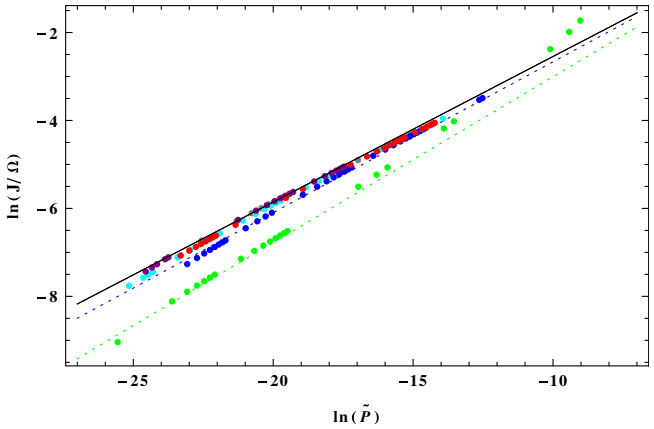

FIG. 10. Leading-order power-law scaling of the black-hole angular momentum divided by the initial angular velocity, J/Ω. The solid black line shows the theoretical prediction given by the theoretical value $\lambda_1 = 7/81$ (see Table II), while the dotted colored lines show theoretical predictions with *ad hoc* values of $\lambda_1 = 0.017$ and -0.18 for the vertical sequences $\Omega = 0.1$ (blue) and $\Omega = 0.3$ (green).

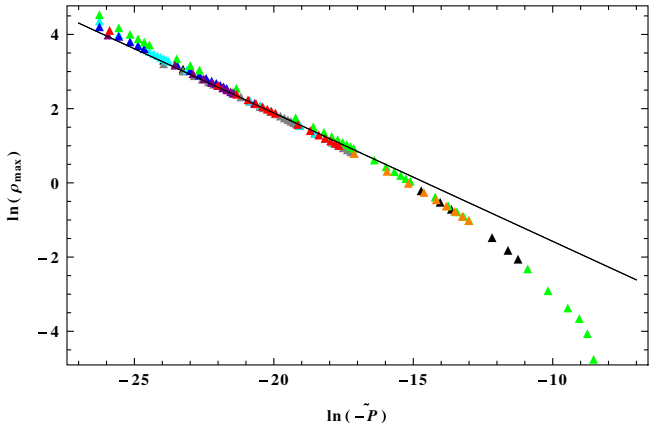

FIG. 11. Leading-order power-law scaling of the maximum central density $\rho_{\max}$, now for the subcritical halves of the same sequences of initial data, and hence plotted against $\ln(-\tilde{P})$.

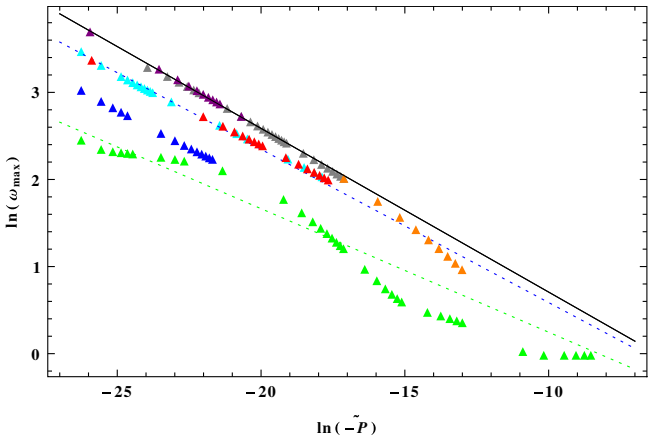

FIG. 12. Leading-order power-law scaling of the maximum central angular velocity, divided by the initial angular velocity, $\omega_{\max}/\Omega$. The dotted colored lines use the same heuristic λ_1 as in Fig. 10.

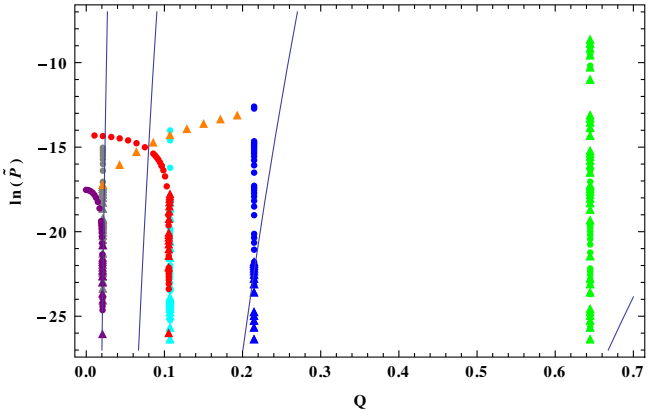

FIG. 13. Our initial data in the $Q\tilde{P}$ plane. As $|\tilde{P}|$ becomes very small near the black-hole threshold, we plot $\ln|\tilde{P}|$ rather than $\tilde{P}$. Different one-parameter sequences of initial data are color coded as in Table III, with dots denoting supercritical data and triangles subcritical data. The solid curves are given by $|\tilde{P}| = |Q/b_1|^{1/\epsilon}$, for $b_1 = 0.03$, 0.1, 0.3 and 1 (from left to right). Hence all our data obey $|\tilde{P}| > |Q/b_1|^{1/\epsilon}$ for $b_1 \geq 1$.

3. Breakdown of scaling?

We do not see any breakdown of scaling. To get at least some idea of whether we should expect one at our level of fine-tuning, we replace the condition (36) for scaling to break down by $|\tilde{P}| < |Q/b_1|^{1/\epsilon}$. We do not know the value of b_1, but Fig. 13 shows that this latter condition is not met for any of our initial data as long as $b_1 > 1$. (We have used the exact value of λ_1 in ϵ here. For a smaller but still positive heuristic λ_1 even more fine-tuning would be required, while for $\lambda_1 < 0$ we do not expect scaling to break down at all.)

4. Beyond leading order

As we discussed above, our numerical data can be fit to the power laws (42a)–(42d) quite well, at least for modest values of Ω, but these fits require adopting heuristic and Ω-dependent values of the Lyapunov exponent λ_1. We now ask whether, alternatively, the observed behavior of the numerical data can be explained by higher-order terms in the scaling functions $\tilde{F}_J(\tilde{\delta})$ and $\tilde{F}_\rho(\tilde{\delta})$. In the following we will therefore adopt the theoretical value $\lambda_1 = 7/81$ [see Eq. (17)] and will examine deviations of the numerical data from power laws.

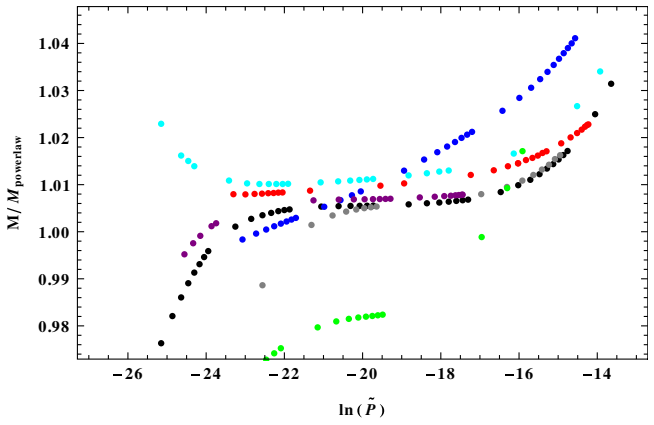

FIG. 14. Black hole masses M with the expected leading-order power law taken out, plotted against $\ln\tilde{P}$. We have cut off data far from the black-hole threshold, where the deviations from the expected power law are large (compare Fig. 9).

To see the deviations from the leading-order power laws more clearly, we plot the ratio of the observed quantities over the predicted leading-order power law. For example, plotting $M/\tilde{P}^{\gamma_M}$ should give $\tilde{F}_M$. This is illustrated in Figs. 14 through 17. In these figures we again show $\ln|\tilde{P}|$, that is logarithmic distance from the black-hole threshold, on the horizontal axis. In contrast to the previous plots, where we showed all our data points, we now restrict ourselves to $\ln|\tilde{P}| < -12$ to discard the data furthest from the black-hole threshold.

Figure 14 shows that the deviations of M from the leading-order power law are at the level of a few percent (after removing data which are far from the black-hole threshold), so that we would not be able to distinguish these deviations from numerical error. The smallness of the deviation is consistent with $\tilde{P}(\eta, \Omega)$ being well approximated by $C_0(\eta - \eta_*)$ and $KC_1^2(\Omega_*^2 - \Omega^2)$ on vertical and horizontal sequences, respectively, and at the same time $\tilde{F}_M(\tilde{\delta})$ being well approximated by its leading-order term, namely 1. It is of course possible that both approximations are violated with the violations largely canceling out, but this seems implausible.

For $\rho_{\max}$, the deviations are significantly larger (Fig. 16), and larger again for J (Fig. 15) and $\omega_{\max}$ (Fig. 17). It is possible that these deviations are caused by higher-order terms in the scaling functions. However, for $\rho_{\max}$ there seems to be no clear systematic effect, and it may be that the deviations from unity can be explained by numerical error

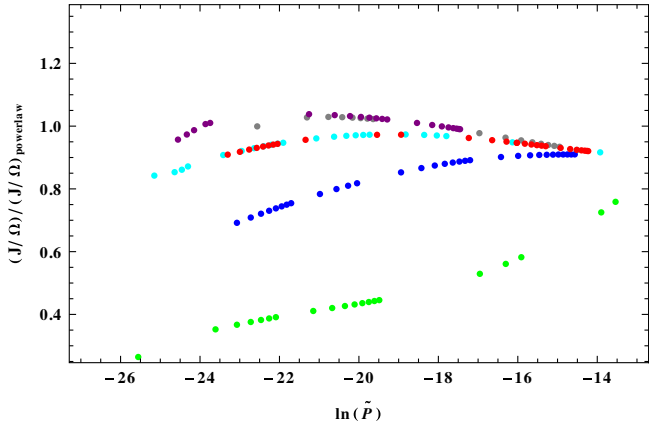

FIG. 15. Values of J/Ω with the expected leading-order power law taken out.

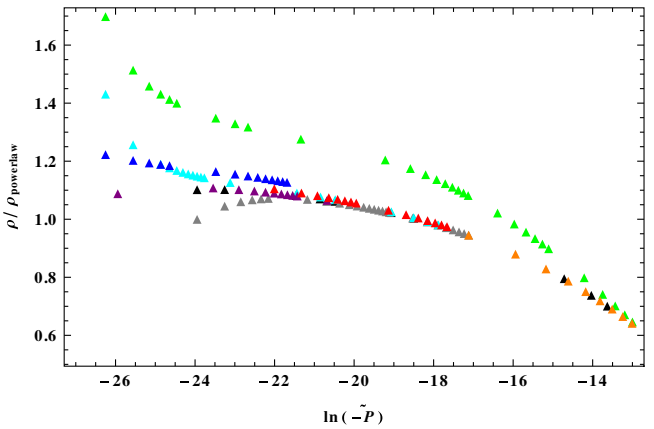

FIG. 16. Maximum densities $\rho_{\rm max}$ with the expected leading-order power law taken out, plotted against $\ln(-\tilde{P})$.

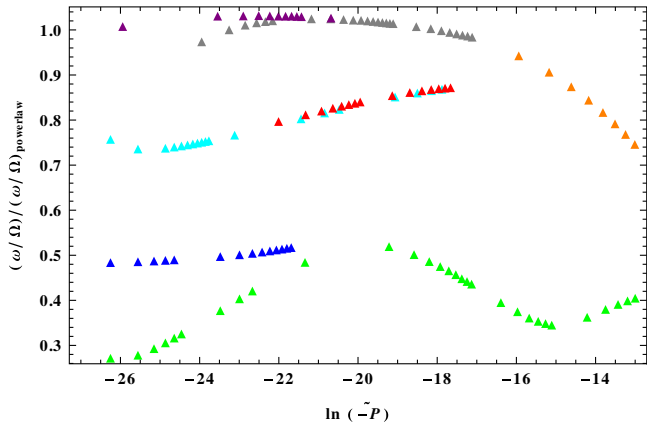

FIG. 17. Values of $\omega_{\rm max}/\Omega$ with the expected leading-order power law taken out.

at large fine-tuning (and small scales), and by a breakdown of our theory at $\Omega = 0.3$ far from the black hole threshold.

For J/Ω and $\omega_{\rm max}/\Omega$ there does seem to be a systematic effect. We find that these quantities are systematically

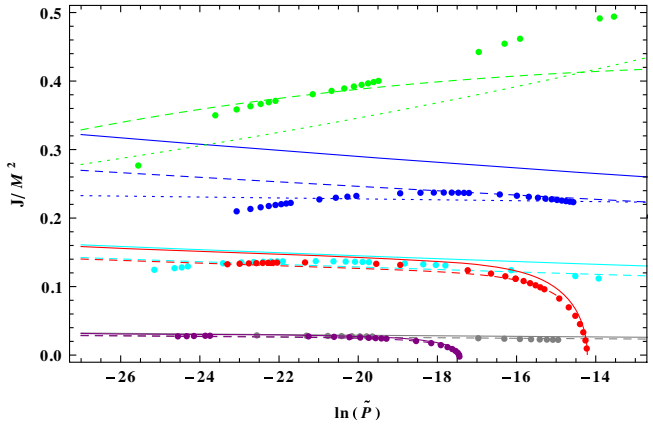

FIG. 18. Numerical values of J/M^2 (dots), $\tilde{\delta}$ as computed from Eq. (39) with the theoretical value of λ_1 (solid lines), $\tilde{\delta}$ with the heuristic values of λ_1 for $\Omega = 0.1, 0.3$ (dotted lines), and the heuristic fit (59) for $\tilde{F}_{J/M^2}(\tilde{\delta})$ (dashed lines), all plotted against $\ln\tilde{P}$.

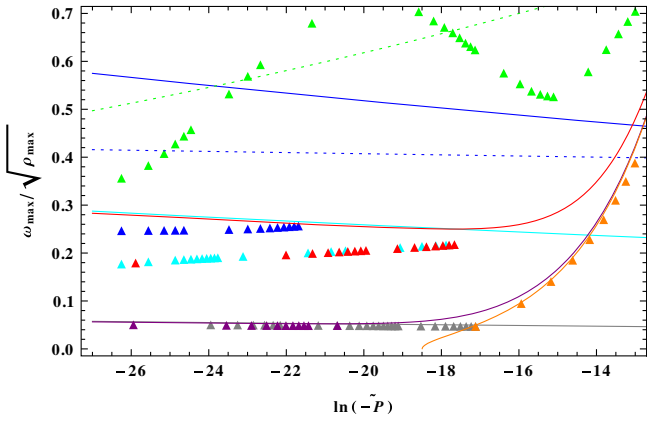

FIG. 19. Numerical values of $\omega_{\rm max}/\sqrt{\rho_{\rm max}}$ (triangles), $(c_\omega/\sqrt{c_\omega})\tilde{\delta}$ with the theoretical value of λ_1 (solid lines) and the heuristic values of λ_1 for $\Omega = 0.1,\ 0.3$ (dotted lines), all plotted against $\ln(-\tilde{P})$. For clarity, we have restricted the plotting range so that the solid green line (at $\delta \sim 1.5$) is outside the frame.

smaller than our leading-order power-law prediction with increasing Ω.

To investigate these possible systematic effects in the black-hole angular momentum (for supercritical data) and maximal central angular velocity (for subcritical data), we now focus on the related dimensionless quantities J/M^2 and $\omega_{\rm max}/\sqrt{\rho_{\rm max}}$. These quantities can be measured directly, unlike the ratios between measurement and leading-order prediction shown in Figs. 14 through 17. Moreover, J/M^2 and $\omega_{\rm max}/\sqrt{\rho_{\rm max}}$ should depend on $\tilde{\delta}$ only. The results are shown in Figs. 18 and 19 (colored dots and triangles). The horizontal axis is again logarithmic distance to the black-hole threshold. Note that to leading order we expect $J/M^2 \simeq \tilde{\delta}$, and $\omega_{\rm max}/\sqrt{\rho_{\rm max}} \simeq (c_\omega/\sqrt{c_\rho})\tilde{\delta}$.

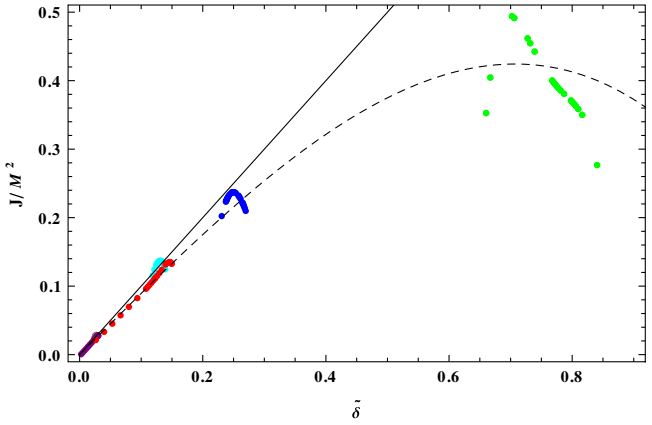

FIG. 20. Numerical values of J/M^2 (dots), $\tilde{\delta}$ (solid black line) and the heuristic fit (59) for $\tilde{F}_{J/M^2}(\tilde{\delta})$ (dashed black line), all plotted against $\tilde{\delta}$.

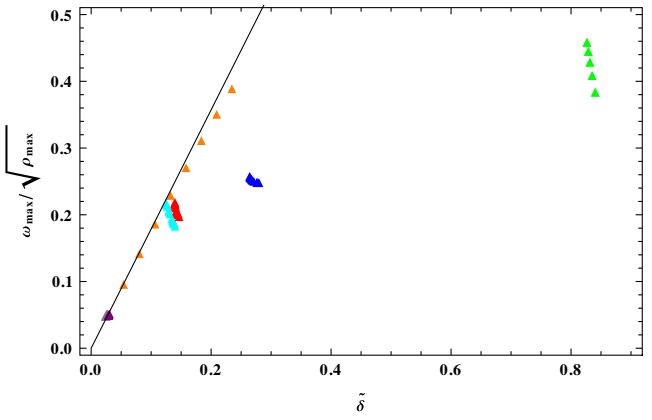

FIG. 21. Numerical values of $\omega_{\max}/\sqrt{\rho_{\max}}$ (triangles) and $(c_\omega/\sqrt{c_\rho})\tilde{\delta}$ (solid black line), all plotted against $\tilde{\delta}$.

Our first observation is that both J/M^2 and $\omega_{\max}/\sqrt{\rho_{\max}}$ depend strongly on the sequence of initial data, but very little on distance to the black-hole threshold within each sequence. Consistently with that, we find that the two pairs of one horizontal and one vertical sequence intersecting on the black-hole threshold (grey and purple, cyan and red) are very close to each other.

The reason for this is simply that $\epsilon \simeq 0.015$ is small, as we see by also plotting $\tilde{\delta}$, as computed from Eq. (39) with the approximations (51) through (54) (solid colored lines). While $\tilde{\delta}$ increases towards the black-hole threshold (towards the left), it does so very slowly for the degree of fine-tuning we can achieve.

As a consequence, modulo numerical error, each vertical one-parameter sequence of initial data gives us essentially only a single point when we plot our estimates of $\tilde{F}_{J/M^2}$ and $\tilde{F}_{\omega/\sqrt{\rho}}$ against $\tilde{\delta}$ in Figs. 20 and 21. Given that $\tilde{F}_{J/M^2}$ has to be an odd function in $\tilde{\delta}$, a reasonable attempt at such a fit is

$$\tilde{F}_{J/M^2}(\tilde{\delta}) \simeq \tilde{\delta} - (0.1)\tilde{\delta}^3 - (0.6)\tilde{\delta}^5, \tag{59}$$

shown as the dashed line in Fig. 20. We have compromised between using the two fitting parameters to improve the fit of the lower-angular-momentum sequences (gray, purple, cyan, red), and a very rough fit of the two high-angular-momentum sequences (blue, green). The resulting theoretical predictions are also included as dashed colored lines in Fig. 18.

Plotting $\omega_{\max}/\sqrt{\rho_{\max}}$ against $\tilde{\delta}$ does not give a consistent $\tilde{F}_{\omega/\sqrt{\rho}}(\tilde{\delta})$ at all; see Fig. 21. The orange sequence is well fitted by $\tilde{F}_{\omega/\sqrt{\rho}} = \tilde{\delta}$, as are the gray/purple sequences (which effectively only contribute one point). By contrast, the cyan/red, blue and green sequences (each contributing effectively only one point) completely disagree with this, even if we use the heuristic values of λ_1 for $\Omega = 0.1, 0.3$.

Besides "heuristic" values of λ_1 and nontrivial scaling functions, another possibility for making the theoretical values for J and $\omega_{\max}$ agree better with our simulations is to go to the next order in $Q(q,p)$, that is

$$Q(\Omega,\eta) \simeq C_1\Omega[1 + C_2(\eta - \eta_{*0}) + C_3\Omega^2]. \tag{60}$$

Recall that we consider Ω^2 and $\eta - \eta_{*0}$ as being of the same order of smallness. We have now expanded Q to $O(\Omega^3)$ and, as before, P to $O(\Omega^2)$. In particular, in a first step we might hope to find a value of C_3 that would improve the agreement of J/M^2 and $\omega_{\max}/\sqrt{\rho_{\max}}$ for $\Omega = 0.1$ and $\Omega = 0.3$ with the predicted values. However, the fit for these four data points cannot be improved by a single consistent choice of C_1, even roughly: the relative deviations for $\Omega = 0.3$ are not 9 times larger than those for $\Omega = 0.1$, and the relative deviations of J/M^2 and $\omega_{\max}/\sqrt{\rho_{\max}}$ are not the same. Hence this refinement of the theory on its own also does not appear to be promising.

Of course, all attempts to improve the agreement between numerical results and the predicted scaling assume that the evolution still goes through a Phase II. In accordance with our earlier discussion, it is possible that, for $\kappa < 1/9$ and sufficiently large Ω, this is no longer the case.

V. CONCLUSIONS

We have studied the critical collapse of a rotating perfect fluid for different values of the equation-of-state parameter κ, generalizing our earlier results for the radiation fluid defined by $\kappa = 1/3$. Varying κ is interesting because, for $\kappa < 1/9$, we expect the self-similar critical solution to have two, rather than one, unstable modes. Moreover, the second mode is controlled by angular momentum in the initial data, and in turn controls angular momentum in the final outcome. We have generalized the theory to accommodate this second unstable mode in a manner that treats both growing modes on an equal footing.

With two growing modes, we expect qualitatively different behavior near the black-hole threshold. This is because the attracting manifold of the critical solution, which is codimension two in the space of initial data, is now only a submanifold of the black-hole threshold, which is always codimension one. Hence by fine-tuning a generic one-parameter family of initial data to the black-hole threshold, we cannot set both growing modes to zero. In particular we have two key expectations:

(1) A breakdown of the well-known power-law scalings at sufficient fine-tuning, below some scale set by the position along the black-hole threshold (distance from the attracting manifold of the critical solution).
(2) The modification of the leading-order power laws by universal scaling functions.

We have also performed numerical simulations of the collapse of rotating perfect fluids. For supercritical evolutions we measured the black-hole mass M and angular momentum J, while for subcritical evolutions we introduced the maximum central rotation rate $\omega_{\max}$ as a diagnostic for critical collapse. The latter mirrors the scaling of the black-hole angular momentum J similar to how the maximum central density $\rho_{\max}$ mirrors the scaling of the black-hole mass M (see Ref. [13]).

We found that M and J as well as $\rho_{\max}$ and $\omega_{\max}$ are well approximated by power laws, for $\kappa > 1/9$ as well as $\kappa < 1/9$, at least as long as the initial rotation rate Ω is sufficiently small. In particular, we did not observe the minimum scale discussed above. Unless $b_1 \ll 1$ in the nonlinearity ellipse (26), this is not in contradiction with the theory, basically because the second unstable mode grows much more slowly than the first one. Observing the minimum scale would require significantly better fine-tuning than we can currently afford.

We did observe some apparently systematic deviations from power-law scaling for the black-hole angular momentum J (in supercritical evolutions) and maximal angular rotation rate $\omega_{\max}$ (in subcritical evolutions). However, our numerical observations did not give us enough data points to make quantitative predictions about hypothetical scaling functions, and our subcritical data did not seem to define a consistent scaling function for $\omega_{\max}$.

An alternative, but at the moment purely heuristic approach, is to assume that the Lyapunov exponent of the second unstable mode takes heuristic values that decrease with increasing initial rotation rate. This might be justified by nonlinear effects, but modeling these would go far beyond our current theoretical model. We note that the authors of Ref. [14] found similar changes in Lyapunov exponents in the aspherical collapse of massless scalar fields. However, while the authors of Ref. [14] reported that large deformations render an aspherical $l = 2$ mode unstable, we found that larger Ω makes the aspherical $l = 1$ more stable.

In summary, our numerical results are in agreement with the theory, but so far we have been unable to make quantitative predictions about key elements of the theory, including the scaling functions. We believe that three different approaches could improve this in future work.

First, the universality of the scaling functions we have fitted could be tested by carrying out numerical evolutions of one or more other two-parameter families of initial data. The same applies for the universality of the conjectured heuristic values of λ_1. It would be interesting to examine two-parameter families of initial data which, at $q = 0$, have zero angular momentum but are not spherically symmetric, and we should test the hypothesis that, for $\kappa > 1/9$, critical scaling is seen for *any* initial data sufficiently close to the black-hole threshold, including rapidly spinning data.

Second, the hypothesis of a minimum scale could be tested by much better fine-tuning to the black-hole threshold. This requires higher numerical resolution, which could be achieved either with more sophisticated regridding schemes, or perhaps a gauge condition that makes the coordinate system shrink approximately with the critical solution, or adaptive mesh refinement.

Third, the universal scaling functions could be determined directly by evolving a single one-parameter family of initial data, consisting of the critical solution with the two unstable perturbations in different ratios, at an amplitude that is just about to become nonlinear; see Eq. (28). This will require constructing initial data for the critical solution and its perturbations. Success in this approach would mean that we had fewer free parameters to fit and so would make our theory more predictive.

A key theoretical prediction is that exactly at the black-hole threshold J/M^2 and $\omega_{\max}/\sqrt{\rho_{\max}}$ each take a universal limit, even if there is a minimum scale [11]. Evolving the initial data (28) with $\alpha = \alpha_*$ would directly tell us these universal values. Moreover, in principle it is possible that the universal scaling functions $F_M \to 0$ and $F_\omega \to 0$ as $\alpha \to \alpha_*$, which means that the space of initial data that form naked singularities could be the entire black-hole threshold (codimension one), rather than the attracting manifold of the critical solution (codimension two).

ACKNOWLEDGMENTS

This work was supported in part by NSF Grants No. PHY-1402780 and No. 1707526 to Bowdoin College.

[1] M. W. Choptuik, Phys. Rev. Lett. **70**, 9 (1993).
[2] C. R. Evans and J. S. Coleman, Phys. Rev. Lett. **72**, 1782 (1994).
[3] A. M. Abrahams and C. R. Evans, Phys. Rev. Lett. **70**, 2980 (1993).
[4] C. Gundlach, Living Rev. Relativity **10**, 5 (2007).
[5] T. W. Baumgarte and C. Gundlach, Phys. Rev. Lett. **116**, 221103 (2016).
[6] C. Gundlach and T. W. Baumgarte, Phys. Rev. D **94**, 084012 (2016).
[7] D. W. Neilsen and M. W. Choptuik, Classical Quantum Gravity **17**, 761 (2000).
[8] T. Koike, T. Hara, and S. Adachi, Phys. Rev. Lett. **74**, 5170 (1995).
[9] D. Maison, Phys. Lett. B **366**, 82 (1996).
[10] C. Gundlach, Phys. Rev. D **65**, 084021 (2002).
[11] C. Gundlach, Phys. Rev. D **65**, 064019 (2002).
[12] S. L. Liebling, Phys. Rev. D **58**, 084015 (1998).
[13] D. Garfinkle and G. C. Duncan, Phys. Rev. D **58**, 064024 (1998).
[14] M. W. Choptuik, E. W. Hirschmann, S. L. Liebling, and F. Pretorius, Phys. Rev. D **68**, 044007 (2003).
[15] T. W. Baumgarte and P. J. Montero, Phys. Rev. D **92**, 124065 (2015).
[16] T. Nakamura, K. Oohara, and Y. Kojima, Prog. Theor. Phys. Suppl. **90**, 1 (1987).
[17] M. Shibata and T. Nakamura, Phys. Rev. D **52**, 5428 (1995).
[18] T. W. Baumgarte and S. L. Shapiro, Phys. Rev. D **59**, 024007 (1998).
[19] T. W. Baumgarte, P. J. Montero, I. Cordero-Carrión, and E. Müller, Phys. Rev. D **87**, 044026 (2013).
[20] T. W. Baumgarte, P. J. Montero, and E. Müller, Phys. Rev. D **91**, 064035 (2015).
[21] J. D. Brown, Phys. Rev. D **79**, 104029 (2009).
[22] E. Gourgoulhon, *3+1 Formalism in General Relativity* (Springer, New York, 2012).
[23] C. Bona, J. Massó, E. Seidel, and J. Stela, Phys. Rev. Lett. **75**, 600 (1995).
[24] M. Alcubierre, B. Brügmann, P. Diener, M. Koppitz, D. Pollney E. Seidel, and R. Takahashi, Phys. Rev. D **67**, 084023 (2003).
[25] M. Thierfelder, S. Bernuzzi, and B. Brügmann, Phys. Rev. D **84**, 044012 (2011).
[26] M. Shibata and K. Uryū, Phys. Rev. D **62**, 087501 (2000).
[27] O. Dreyer, B. Krishnan, D. Shoemaker, and E. Schnetter, Phys. Rev. D **67**, 024018 (2003).